EXPERIMENTAL STUDY AND COMPUTATIONAL TURBULENCE MODELING OF COMBINED RAYLEIGH–TAYLOR AND KELVIN–HELMHOLTZ MIXING WITH COMPLEX STRATIFICATION

A Thesis

by

THOMAS PATRICK FINN

Submitted to the Office of Graduate and Professional Studies of
Texas A&M University
in partial fulfillment of the requirements for the degree of

MASTER OF SCIENCE

Chair of Committee,	Devesh Ranjan
Committee Members,	J.N. Reddy
	Helen Reed
	Oleg Schilling
Head of Department,	Andreas Polycarpou

August 2014

Major Subject: Mechanical Engineering

ABSTRACT

An experimental study of the combined Rayleigh–Taylor instability (RTI) and Kelvin–Helmholtz instability (KHI) is presented at three different Atwood numbers (0.05, 0.971, 0.147) and multiple velocity ratios to examine the morphological development of the flow field. The Atwood number is the ratio of the difference between the densities of the heavy and light streams to their sum. These experiments were performed using the multilayer gas tunnel facility at Texas A&M University. The tunnel is a convective type system, where gases of different densities flow parallel to one another and are separated by a splitter plate until mixing is allowed downstream in the test section. Three-wire hot-wire probe and particle-image velocimetry (PIV) diagnostic techniques are used to set the velocities in the experiments. Visualization is performed using a high resolution digital camera by injecting fog into one of the streams and collecting scattered light from the illuminated fog particles. Shear effects on the complex stratification are studied. Complex stratification occurs when there is a non-constant density profile in the light fluid mixture, while the constant density profile case is referred to as generic stratification. Transition was found to occur between Richardson numbers of -0.25 and -1.0. Additionally, two different scenarios with and without complex stratification are examined through the mixing layer growth and the non-dimensional growth rate parameter $\alpha_{b,s}$. Complex stratification was found to produce higher mixing layer growth and larger values of $\alpha_{b,s}$ than generic stratification.

The stratification experiments were also simulated using a one-dimensional, two-equation K–ε Reynolds–averaged Navier–Stokes (RANS) model in collaboration with Lawrence Livermore National Laboratory (LLNL). The model is implemented in a

hydrodynamics code using a third-order weighted essentially non-oscillatory (WENO) or central differencing method for the advection terms, a second-order central differencing method for the gradients in the source, sink, and diffusion terms, and a second-order implicit Crank–Nicolson (CN) method for the time evolution. Simulations are compared to experiments through the mixing layer and non-dimensional growth parameter $\alpha_{b,s}$. The overall trends shown by the simulations were consistent with experimental data. Specific values for growth height and $\alpha_{b,s}$, however, were found to be vastly under predicted.

DEDICATION

To my late grandfather and friend, John B. Finn Jr.

ACKNOWLEDGEMENTS

There are far more people than I can name that have helped me get to where I am today. Without their constant support and encouragement the work presented in this thesis would not be possible. First and foremost, I would like to thank my advisor Dr. Devesh Ranjan for offering me the opportunity to work in his lab, and provide the essential resources needed to complete this work. In addition, I would like to thank him for all he has taught me, both inside and outside the classroom. Without his guidance, I would not be the researcher or professional engineer that I am today.

Next I would like to thank my many lab mates. There constant support and help at a moments notice proved invaluable in getting research done. Dr. Jacob McFarland has provided me with sound advice on countless problems both within research and in everyday life. Bhanesh Akula has provided me with the strong foundation required in order to further our research. Sarat Kuchibhatla has been a good friend, and has always ensured the quality of my work. David Reilly, Sandeep Pidaparti, Skylar Creel, and Eric Umagar have also kept me sane by relieving stress when required and giving advice when asked.

Dr. Oleg Schilling of Lawrence Livermore National Lab has helped me immensely improve my computational skills, and has provided guidance on the code used in this work. I would like to thank him for his patience with me, and willingness to always work around my schedule.

Finally, I would like to thank my brother Jack Finn for encouraging me to further my education by going to graduate school, and my parents Jack and Patty for always supporting the decisions I made to get where I am today.

TABLE OF CONTENTS

Page

LIST OF FIGURES

FIGURE Page

LIST OF TABLES

TABLE Page

1. INTRODUCTION

1.1 Background

In this work, an experimental investigation of the combined Rayleigh–Taylor and Kelvin–Helmholtz instabilities (RTI and KHI, respectively) has been performed. Additionally, the effect of complex stratification has been studied both experimentally and numerically. The computational studies were conducted in collaboration with Lawrence Livermore National Laboratory (LLNL) using a one-dimensional Reynolds-Averaged Navier–Stokes (RANS) model. Experiments were performed in the multilayer gas tunnel facility at the Texas A&M Shock Tube and Advanced Mixing Laboratory.

1.1.1 Rayleigh–Taylor Instability

The Rayleigh–Taylor instability occurs when two fluids of different densities are accelerated normal to their interface [1, 2]. The unstable orientation causes the pressure gradient to be misaligned with the density gradient, $\vec{\nabla}\rho \cdot \vec{\nabla}p < 0$. This misalignment creates vorticity through the baroclinic term in the inviscid vorticity equation,

$$\frac{D\vec{\omega}}{Dt} = (\vec{\omega} \cdot \vec{\nabla})\vec{V} - \vec{\omega}(\vec{\nabla} \cdot \vec{V}) + \underbrace{\left[\frac{1}{\rho^2}\vec{\nabla}\rho \times \vec{\nabla}p\right]}_{baroclinic\ term} \tag{1.1}$$

where $\vec{\omega}$ is the vorticity vector, $\vec{V}$ is the velocity vector, ρ is the fluid density, p is the pressure, and $\vec{\nabla}$ represents the gradient of a quantity. Thus, the RTI is driven by baroclinic vorticity. The interface is seeded by small initial perturbations which grow exponentially at time progresses, as predicted by linear stability theory [3]. The

growth of the RTI is characterized by the Atwood number,

$$A_t = \frac{\rho_H - \rho_L}{\rho_H + \rho_L} \tag{1.2}$$

where ρ is the density, and subscripts H and L denote the heavy and light fluids respectively. A large difference in density between the fluids corresponds to an Atwood number near 1, and low density differences result in an Atwood number close to 0.

The growth of the mixing layer can be divided into three stages [4]. In stage 1, the perturbation is defined by the most unstable wavelength (λ_m), and drives the initial growth of the mixing layer. This stage lasts approximately until the amplitude of the perturbation reaches $\sim \lambda_m/2$. Stage 2 begins at this point, and a dominant wavelength emerges (λ_d). During stage 2, the mixing layer growth rate decreases and larger structures begin to dominate the mixing region. Dimonte *et al.* [5] have shown that smaller wavelength modes combine to create larger wavelength modes. When λ_d reaches $\sim 10\lambda_m$, stage 3 begins, and memory of the initial conditions is lost. In this stage, the mixing layer grows self-similarly, with a length scale gt^2 where g is gravity and t is time. Within the last twenty years, however, the three stage growth description has been questioned.

The total mixing layer growth in the self similar regime can be characterized by the solution,

$$h_{b,s} = \alpha_{b,s} A_t g t^2 \tag{1.3}$$

where $\alpha_{b,s}$ is a non-dimensional growth parameter and $h_{b,s}$ is the mixing height of the bubbles and spikes, respectively, as characterized by the 5–95% criterion. This measure of the mixing width is determined by using fog as a tracer in one of

the streams, the mixing layer is then measured from 95% to 5% light extinction. In experiments using liquids, dye can be used instead of fog. Tracer particles are illuminated using a LED back light, located behind the test section. The light fluid rising into the heavy fluid is described as a bubble, while the heavy fluid falling down into the light fluid is referred to as a spike. For Atwood numbers ($A_t \lesssim 0.1$), the growth of the bubbles and spikes occurs symmetrically. For higher Atwood numbers, however, it has been observed that the spikes grow faster than the bubbles.

1.1.2 Kelvin–Helmholtz Instability

The Kelvin–Helmholtz instability occurs when two stratified fluids flow tangential to the interface at a velocity ratio other than unity. Whereas the RTI is described by the non-dimensional Atwood number, the KHI is characterized by the velocity ratio or the difference between the velocities,

$$U_r = \frac{U_S}{U_F} \tag{1.4}$$

$$\Delta U = U_F - U_S \tag{1.5}$$

respectively, where subscripts S and F denote the slow and fast velocity streams respectively. The mixing height is determined by

$$h = \beta \, \Delta U \, t, \tag{1.6}$$

where h is the mixing width, β is a dimensionless coefficient, ΔU is the velocity difference between streams, and $t = x/U_m$ is time by Taylor's hypothesis.

Even in a pure RTI case (where the flow has no velocity tangential to the interface), the KHI will develop as a secondary instability from the viscous interactions between

the rising bubbles and falling spikes. This will further promote mixing between the two fluids. In a combined RT and KH instability flow, the parameter of interest is the Richardson number, which is the ratio of potential and kinetic energy [6],

$$R_i = \frac{-g(\frac{\partial \rho}{\partial z})}{\rho(\frac{\partial u}{\partial z})^2} = -\frac{2hg\Delta\rho}{\rho(\Delta U)^2} = -\frac{4ghA_t}{(\Delta U)^2} \tag{1.7}$$

where $2h$ signifies the width of the mixing layer, g and ρ are respectively gravity and mean density, $\Delta\rho$ and ΔU are the differences in density and velocity, and z is the vertical direction (as required for potential energy). The initial Richardson number will be positive for stable RT flow, and negative for unstable flow [6].

1.1.3 Relevance and Applications

The combined Rayleigh–Taylor and Kelvin–Helmholtz instabilities are prevalent in nature and technical applications. For example, the RTI and KHI occur in air/fuel mixing in combustion chambers [7], the outer region of supernovae [8], and in the hydrodynamics of lakes and reservoirs [9]. These instabilities are also prominent in Z-pinch implosions and the compression of the fuel capsule in inertial confinement fusion (ICF), which is the primary motivation for this research [8, 10].

In ICF, high powered lasers are used to heat the outer layer of a target capsule. This outer layer then ablates, accelerating a shock wave into the fuel target which provides the necessary compression for ignition. During this process, the RTI causes interpenetration between the lower density shell and the higher density ablated material [11, 12]. This interpenetration can grow non-linearly, causing the classical RT bubble and spike structures to develop, resulting in an asymmetric pressure drive which produces turbulent mixing between materials [11, 13, 14, 15]. Furthermore, as the RTI grows, secondary KH vortices develop due to the growth of bubble and spike structures [11]. Turbulent KH induced mixing further reduces the yield, which

is one of the limiting factors for ignition of ICF capsules [12].

The growing global energy concern represents one of the defining engineering challenges of our time. If ICF is successful, it could revolutionize the energy industry. Additionally, the modeling of complex flows such as the RTI and KHI remains a challenge for the turbulence community. Current numerical models used to simulate ICF must be validated in order to ensure their accuracy; this validation requires an understanding of the turbulence development. By better understanding how the growth of the instabilities affect the hydrodynamic implosion of the fuel target, it may be possible to manufacture a fuel target that minimizes the growth of the mixing layer. This could increase the yield and lead to ignition of the ICF target capsule.

Currently, the combined Rayleigh–Taylor and Kelvin–Helmholtz instability has not been well studied. Further, neither experiments nor simulations have been conducted with complex stratification. This experimental configuration provides a good test case for simulations and models, and can be used to determine the effect that a non-constant density profile may have on the mixing layer behavior. Complex stratification could be present in ICF capsules due to manufacturing impurities, which may have a significant effect on instability growth.

1.2 Previous Experiments

Throughout the last half century, the Rayleigh–Taylor and Kelvin–Helmholtz instabilities have been studied using a variety of experimental techniques, both individually and combined. In this section, a brief summary of the work leading up to the current research will be provided.

1.2.1 Rayleigh–Taylor Instability

One of the first experimental studies was conducted in 1950 by Lewis [2]. In the experiment a vertical chamber was accelerated downwards with two fluids separated

by a diaphragm. The diaphragm ruptured at the onset of the acceleration, allowing the fluids in the chamber to mix. A similar procedure was used by Emmons *et al.* in 1960 [16]. These early experiments did not allow quantification of the initial conditions, and also introduced particulate matter into the fluid. It was concluded, however, that the early time growth agreed well with linear stability theory.

In an experiment performed by Read [17], a multi-mode perturbation was studied. In this experiment the test chamber was accelerated by a rocket motor, and it was concluded that the best estimate for the self-similar growth parameter, α, is 0.07. Andrews and Spalding [18] proposed orienting the fluids in a stable configuration, and then quickly rotating the test section by 180° to make them unstable. With this setup, a large scale two-dimensional rotational motion was imposed on the interface. This resulted in a reduction of the mix width, and a growth parameter value of 0.04. In yet another experimental setup, Linden *et al.* and Dalziel *et al.* [19, 20, 21] used a plate to initially separate the different fluids, which was then removed to allow mixing. They discovered when removing the plate, that substantial effects were imposed on the early and possibly late stage growth of the mixing layer.

Snider and Andrews [22] studied the RTI in a plexiglass water channel, where the mixing layer grows as the flow moves downstream after initially being separated by a splitter plate. This setup uses water at different temperatures, and therefore different densities, to create the unstable stratification between the two streams. By using cold/hot water, it is only practical to study very low Atwood numbers ($\sim 10^{-3}$). They measured the self-similar growth of the mixing layer using optical techniques, which agreed with the earlier work of Snider and Andrews resulting in a self-similar growth parameter of 0.07.

Using the same water channel, Wilson and Andrews [23] used thermocouples and a temperature marker technique to obtain density data within the mixing layer.

They concluded that there is an inertial range with a $-5/3$ power law, showing the presence of a Kolmogorov microscale where kinetic energy is dissipated by viscous effects. Ramaprabhu and Andrews [24] confirmed this scaling for both density and velocity using thermocouples and PIV.

Banerjee and Andrews [25] constructed a gas channel to investigate the RTI. This facility allowed for a much higher range of Atwood numbers ($0 \leq A_t \leq 0.75$) to be studied since various amounts of helium gas could be premixed with the incoming air stream. Additionally, two hot-wire and digital imaging techniques were used for data collection [25, 26], which will be discussed later in § 2.2.3. Using these techniques, velocity fluctuations were obtained providing the turbulent correlations $\overline{u'^2}$, $\overline{v'^2}$, $\overline{w'^2}$, $\overline{\rho'^2}$, $\overline{\rho' v'}$, where a turbulent fluctuation is defined as

$$q' = q - \overline{q} \tag{1.8}$$

with $\overline{q}$ representing the time averaged value, and q' the fluctuation from this average. Using the same facility, Kraft *et al.* [26] obtained probability density functions ($pdfs$) and energy density spectra for $0.03 \leq A_t \leq 0.04$. Banerjee *et al.* [27] extended this study to an Atwood number of 0.6 using air and an air/helium mixture as the heavy and light fluids, respectively. They concluded that the growth of the bubbles and spikes occurs asymmetrically for Atwood numbers greater than 0.1, and reported an increase in the spike growth rate parameter, α_s.

Mueschke [28] and Mueschke *et al.* [29] used a water channel and salt to create the density gradient between streams ($A_t \sim 7.5 \times 10^{-4}$) to examine the effects of a high-Schmidt-number on molecular mixing, and also used a backlight technique to measure the concentration of the mixture. They found that early time mixing is greatly influenced by the Schmidt number, whereas late time mixing is less dependent.

1.2.2 Kelvin–Helmholtz Instability

The Kelvin–Helmholtz instability, also commonly referred to as the plane mixing layer problem, was first analytically solved by Görtler [30] using Prandtl's hypothesis and assuming a constant eddy viscosity. Liepmann and Laufer [31] performed an experiment using a wind tunnel and hot-wire anemometry to analyze a flow over stagnant air. They concluded that the assumptions made by Görtler *et al.* were incorrect, and found that the kinetic energy production, diffusion and dissipation terms are maximum at the center of the mixing layer. Yule [32] continued this work and extended it to two velocity ratios. Yule further concluded that Görtler's solution neglected the asymmetry of the mixing region, and proposed a solution to this problem. Bell and Mehta [33] used a blower wind tunnel to investigate the initial conditions on the plane mixing layer. They determined a difference of 25% in the linear growth rate for the tripped and untripped initial boundary layers.

Another important area of study in the plane mixing layer problem has been the phenomena of vortex pairing, which occurs when two vortical structures ‘‘pair up" to form one larger vortex. Wygnanski and Fiedler [34] studied the plane mixing layer using a wind tunnel and proposed that the large eddies rotate like a solid body. This was confirmed by Winant and Browand [35], who investigated vortex pairing using a water tunnel and injecting one stream with dye for visualization. They also concluded that the growth of the mixing layer is a result of vortex pairing. Browand and Weidman [36] built upon this work using conditional sampling at moderate Reynolds number. They found that significant increases in the production of the Reynolds stress are associated with vortex pairing. Koochesfahani and Dimotakis [37] observed fluid becoming trapped in the center of the vortical structures, with the amount of entrained fluid increasing during the mixing transition, which is defined

as the point at which a large increase in mixed fluid is observed. Beyond the mixing transition, there is increased fluid mixing due to three-dimensional effects.

Brown and Roshko [38] investigated the effects of a shear mixing layer between two fluids of different densities. They also observed entrained fluid in the center of the vortex, and concluded that the density of the fluids did not have a large effect on the spreading angle, which is associated with the growth of the mixing layer.

1.2.3 Combined Rayleigh–Taylor and Kelvin–Helmholtz Instabilities

There have been numerous experiments on the Kelvin–Helmholtz instability in both stable and unstable stratifications. In stable stratification, Thorpe [39] used a long rectangular test section that would first be rotated to induce the shear layer, and then rotated back to its original orientation. Using shadowgraphy, Thorpe concluded that the initial Richardson number does not affect the final Richardson number. He also found that $R_i \approx 1/3$ at the mix center, and at this point, striations begin to form. This infers a collapse of vertical mixing and re-establishment of dominant vertical density gradients. The vertical length scales of the final mean velocity and density structure depend on the Richardson number at the onset of the instability [40, 41].

Performing experiments in a water channel, Browand and Winant [42] discovered that, independent of the fluid densities, stratification prohibits the vortex pairing phenomenon seen in unstratified shear flows, and therefore causes a decay in turbulence production. In a similar setup, Koop and Browand [43] confirmed the Richardson number of 1/3 at the mix center, originally measured by Thorpe. They also noted that at low initial Richardson numbers ($R_i \lesssim 0.125$), the flow field can be divided into two regions. In the first, turbulent growth results from fluid entrainment and vortex pairing until the point of maximum mixing thickness. At this point the second region begins, where large-scale entrainment processes are suppressed and the flow

relaxes to a non-turbulent state.

Recently, studies on unstable stratification and shear mixing have been conducted. Using a modified version of Koop and Browand's facility, Lawrence *et al.* [44] examined this case at various Richardson numbers and an Atwood number of 0.14. They discovered a transition region from homogeneous growth to a quadratic growth, and concluded that at early times, the flow resembles Kelvin–Helmholtz mixing and later becomes dominated by the Rayleigh–Taylor instability. They also noted that as the Richardson number becomes larger, this transition occurs at earlier times. This result is apparent from equation 1.7. As ΔU becomes smaller (and therefore transition occurs sooner due to a weaker KH component), R_i becomes larger.

In addition to their pure RTI experiments, Snider and Andrews [22, 45] also studied the combined instability at low Atwood numbers (≤ 0.005). They also observed the transition regime as seen by Lawrence *et al.* [44], who found that for larger Richardson numbers, the transition point occurs closer to the splitter plate. Additionally, Snider and Andrews [22], concluded that adding shear to the flow did not contribute to the growth of the mixing layer beyond transition, and that transition occurred for Richardson numbers between -5 and -11.

Akula *et al.* [6] used a gas tunnel facility capable of higher Atwood numbers and velocity ratios than the water channel used by Snider and Andrews. In these experiments, the pure RTI, pure KHI, and the combined instability at an Atwood number of 0.035 and three velocity ratios were analyzed and compared. From these experiments, as with the results from Snider and Andrews [22, 45], it was observed that the addition of shear does little to increase the growth rate of the mixing layer once buoyancy effects become dominant. Additionally, Akula *et al.* suggested that for an Atwood number of 0.035, transition occurs at a Richardson number between -1.5 and -2.5 and that the KHI vortical structures are more effective at molecularly

mixing the fluids along the centerline of the mixing layer than the RTI structures. Additionally, Akula *et. al* mention that for the combined case, the mixing width is calculated by,

$$h = \beta \, \Delta U t + \alpha A_t g t^2 \tag{1.9}$$

where β is the non-dimensional growth height of the shear layer, ΔU is the difference between in velocity between the streams, and $t = x/U_m$ is time (by Taylor's hypothesis).

1.3 Previous Simulations and Modeling

Numerical simulations have also been used extensively to predict the growth of the Rayleigh–Taylor and Kelvin–Helmholtz instability. Many numerical techniques such as large eddy simulation, (LES), direct numerical simulation (DNS), and Reynolds–averaged Navier–Stokes (RANS) models have been employed. In this section, works relevant to the present research will be discussed.

Youngs [4] conducted a monotone integrated large eddy simulation (MILES) using the two-dimensional, incompressible TURMOIL hydrodynamics code to study initial Rayleigh–Taylor perturbation growth of single and multiple wavelengths. The TURMOIL code is a modified Eulerian model that introduces dissipation through numerical truncation errors [46]. Later, Youngs [47] performed a three-dimensional simulation using the TURMOIL3D code to simulate a pure RT case. These simulations resulted in a growth rate parameter, α between 0.04 and 0.05. Youngs suggested that the lost memory of the initial conditions and negligible viscosity dependence could have contributed to the underpredicted values of α.

Linden *et al.* [20] used a similar three-dimensional simulation, and found that the growth rate parameter in the self-similar regime ranged from 0.038 to 0.044, again

underpredicting the experimentally accepted value of 0.07. Linden *et al.* suggested that simulations at a finer grid resolution were required for more accuracy; however, at the time of the publication such computing resources were not available. Again using the TURMOIL3D code Dalziel *et al.* [21] found a disagreement in α between experiments and simulations, and suggested that the experimental mean concentration (ensemble average over multiple experiments) is a better characterization of the flow than the growth parameter, α.

Ramaprabhu and Andrews [48] also used MILES to simulate the Rayleigh–Taylor instability. They used the velocity fluctuations at the centerline of the mixing layer to obtain the growth parameter, and similar to the simulations discussed above, reported a smaller growth parameter than measured experimentally. Ramaprabhu and Andrews suggested that the reason for the smaller growth parameter was because experiments have velocity perturbations that accelerate the initial density interface. This hypothesis was then tested, and resulted in better agreement between experimental and numerical results, showing $\alpha \approx 0.06$.

Ristorcelli and Clark [49] used direct numerical simulations in their analysis of the RTI. They proposed that the flow is not self-similar (i.e., that only one length scale describes the flow) and that the growth parameter α, is not a universal constant. Rather, different length scales must be used for each of the three turbulent scales (energy-containing length scale, Taylor microscale, and Kolmogorov dissipation scale).

Banerjee *et al.* [50] used the Besnard–Harlow–Rauenzahn (BHR) three-equation k–S–a model (equations for turbulent kinetic energy, dominant eddy length scale, and mass flux, respectively) to simulate the Rayleigh–Taylor and Kelvin–Helmholtz instabilities separately. These simulations modeled the Bell and Mehta experiments [33] and the previous Banerjee and Andrews experiments [25]. The simulation gave good agreement with the velocity profile and the turbulent kinetic energy in the

Kelvin–Helmholtz case and matched the volume fraction and turbulent mass flux well in the Rayleigh–Taylor case. Other parameters such as the growth rate of the mixing layer were not given.

In addition to their experimental work with the water channel, Snider and Andrews [51] simulated the combined instability using a two-equation, two-dimensional K–ε RANS model. First, they conducted a one-dimensional analysis of the pure Rayleigh–Taylor instability. They reported, depending on turbulent model coefficients, α values between 0.05 and 0.077. For further simulations, the turbulent model coefficients were set to give the corresponding $\alpha = 0.07$ value. Two-dimensional pure RTI and KHI simulations were then conducted and compared to experimental data. Snider and Andrews then combined the buoyancy and shear mixing cases and discovered that adding shear to the flow did not increase the mixing layer growth, but decreased it. They attributed this to the skewing (due to shear) of the normally vertical Rayleigh–Taylor bubbles and spikes. These simulations were carried out at low Atwood numbers and velocity differences (2–5 cm/s).

Olson *et al.* [52] also simulated the combined instability using large eddy simulations. They observed that adding shear changes the motion of the vortical structures from the circular Rayleigh–Taylor vortices to increasingly two-dimensional rollers. They arrived at the same conclusion as Snider and Andrews in that addition of small amounts of shear reduce the mixing rate during the early non-linear regime. Olson *et al.* proposed that the reduction in the mixing rate is due to less energy being channeled into vertical mixing up to the minimum mixing rate. Further addition of shear increases the amount of energy available and the mixing rate will again increase.

Mueschke and Schilling [53] used direct numerical simulation and initial conditions from previous experimental work [54] to model the Rayleigh–Taylor instability. They

concluded that by using experimentally measured initial conditions, the simulation data agreed well with experimental statistics and that in order to accurately simulate a Rayleigh–Taylor mixing experiment, the initial conditions must be known. The simulation data was also used to examine the structure of mean and turbulent transport and mixing [55].

1.3.1 Objectives for this Work

The objective of this work is to further study the combined Rayleigh–Taylor and Kelvin–Helmholtz instability, and specifically:

1. Build upon the work by Akula *et al.* [6], where transition for the combined instability case was found to range between -1.5 and -2.5. By examining a larger set of Atwood numbers, it will be possible to confirm whether these values are true.

2. Provide experimental data to quantify the effect of a complex stratified flows, using the mixing layer and non-dimensional growth parameter $\alpha_{b,s}$ for comparison to a generic stratification.

3. Further develop the Reynolds–averaged Navier–Stokes model at Lawrence Livermore National Laboratory to include the Crank–Nicolson method for the time evolution: this allows the code to use larger time steps by bypassing the CFL condition, and thus, will provide data at later times. This code will then be used to produce initial simulation results in pure RT case with both generic and complex stratifications.

The present work builds upon the experimental and numerical works described above by investigating the effects of a higher Atwood number and velocity ratios. The experimental facility along with the diagnostics used to accomplish this will be

described in the next section, followed by a description of the code. Experimental and numerical results will then be presented and compared. Finally, conclusions will be discussed, as well as future work.

2. EXPERIMENTAL WORK

The following section will discuss the experimental work completed, including the experimental apparatus used, the procedure for conducting experiments, the problem setup, and the results obtained from the test cases.

2.1 Experimental Apparatus

The experimental data presented in this work was obtained using the multilayer gas tunnel facility in the Shock Tube and Advanced Mixing Laboratory (STAML). The gas tunnel was initially designed by Ph.D student and lab mate Bhanesh Akula in an attempt to construct an improved facility compared to the one used by Banerjee, Andrews, and Kraft [25, 26, 27]. A schematic of the facility is shown in figure 2.1. The gas tunnel is an open circuit suction tunnel, powered by a Joy Series 2000 model 38-21-1770CP axivane fan. The facility is capable of $A_t \lesssim 0.84$ and velocities in excess of 5 m/s. All contraction sections are constructed of sheet metal (sections B, D, E, and F), the test section is made of acrylic, and structural supports are square steel tubes. The splitter plates used to separate the streams are made of aluminum.

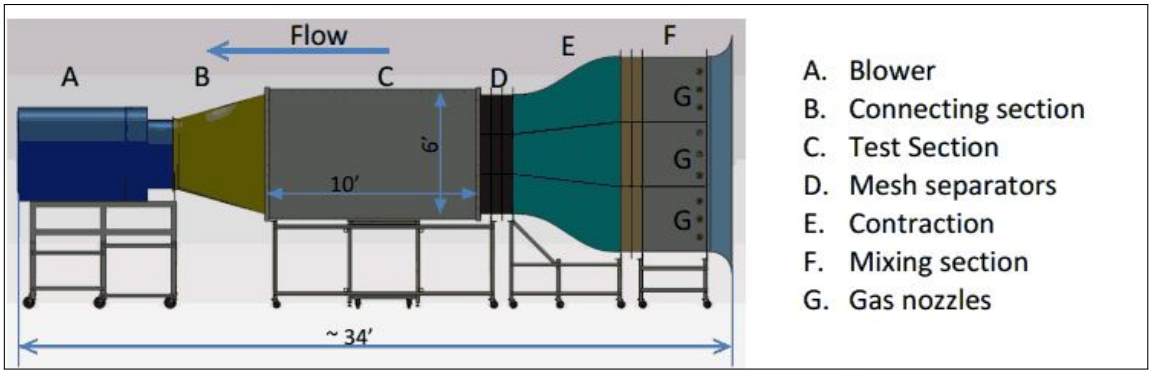

Figure 2.1: CAD model of facility. The flow direction shown corresponds to x, while the vertical direction is y and z is in and out of the page.

The main tunnel is made up of three sub-streams, each measuring 91.44 *cm* by 91.44 *cm* at the inlet (section F). These sub-streams each have independently operated louvers at the tunnel entrance to control the flow velocity through the respective stream, which allows shear to be introduced into the flow field between the fluid streams. Additionally, section F also has baffles, mixing fans, and a honeycomb to first mix the fluids and then disperse the circulation induced by the fans. The splitter plate terminates at the inlet of the test section (C), where all sub-streams are allowed to mix. Prior to the test section is a mixing contraction (E) and a series of wire screen separators (D). The screens (3 total) become finer further downstream and are used to reduce the turbulence levels within the gas before entering the test section by dissipating large eddy structures. An in depth study has been conducted to determine the proper size of the meshes [56]. The furthest upstream screen has 14.17 by 14.17 meshes per *cm* with a wire diameter of 0.01651 *cm* The next two screens (moving downstream) are 19.69 by 19.69 and 23.62 by 23.62 with diameters of 0.01143 and 0.00889 *cm* respectively. Additionally, the meshes increase the uniformity of the flow.

The test section walls, floor, and ceiling are made from 1.27 *cm* thick acrylic

sheets, as transparency is required for light extinction and particle-image velocimetry diagnostic techniques. These acrylic sheets are joined together using 6061 aluminum L bars and fastened with $1/4 - 20$ and M6 bolts. The dimensions of the test section measure 3.048 m long by 1.83 m high and 0.61 m wide. Further, the ceiling of the test section has three parallel slots machined in the acrylic which allows a traverse arm to be lowered into the channel at various span-wise locations. The traverse is supported by two square aluminum tubes that run the length of the test section and can be seen in figure 2.2(a).

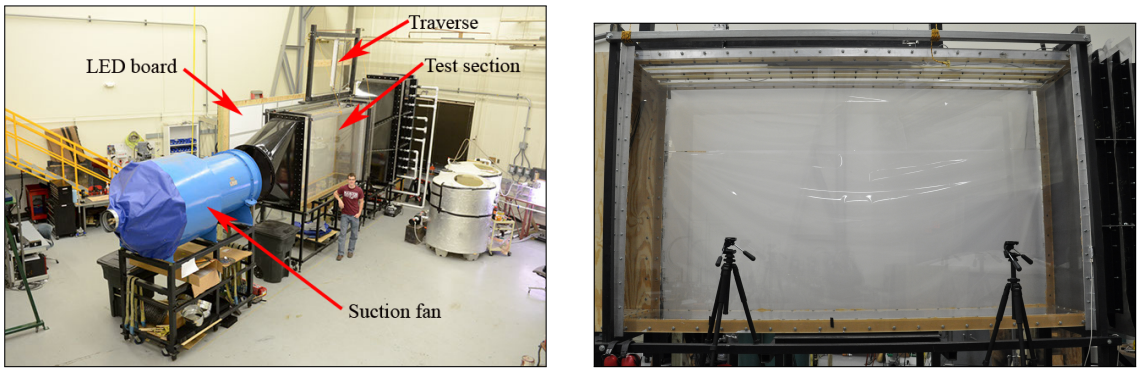

(a) Original gas tunnel setup at STAML.

(b) Test section with two camera tripod mounts at two x locations used for PIV experiments.

Figure 2.2: Configuration of gas tunnel before modifications (a) and test section (b).

Downstream of the test section, the flow passes through another honeycomb in the contraction (section B in figure 2.1) which reduces the vorticity that can be imposed by the fan on the upstream fluid. This helps to reduce the three dimensionality of the flow.

To create the required unstable fluid stratification for an experiment, various gases must be injected and premixed with air in the sub-sections of the tunnel. This is achieved using an intricate PVC piping configuration to bring the gas from compressed gas bottles [see figure 2.3(a)] into the upstream mixing section (F). In each sub-stream of section F, there are three injection pipe systems. Each system consists of three tubes with numerous holes, which distribute the helium throughout the sub-stream. Depending on the conditions of the experiment, up to three gas injection lines can be used, each with six gas bottle connections. For a complex stratification experiment, only helium is hooked up to the bottle connections. This allows pure helium to be injected into section F, causing pockets of helium to rise up to the splitter plate and giving the complex density profile. For generic stratification in the classical Rayleigh–Taylor case, one of the vacant gas lines will be outfitted with nitrogen. With this setup, a mixture of helium is injected into section F, resulting in a uniform density profile across the bottom stream.

An orifice divides the high and low pressure sides of the injection lines and controls the amount of gas allowed into the tunnel (and therefore sets the Atwood number). From one-dimensional gas dynamics, the choked mass flow rate through the orifice is controlled by the upstream total pressure and the orifice area. The total pressure is changed using two pressure regulators, and various orifices can be used to change the area. A table giving the corresponding orifice size and Atwood number is given in [56]. The high pressure section of the lines are made from 1.27 cm stainless steel tubing, while the low pressure sides are constructed of 5.08 cm PVC.

Valves are opened and closed accordingly in order to inject the gas into the appropriate sub-section (bottom, middle, or top) and shown in figure 2.3(b). As mentioned earlier, each sub-section uses baffles along with circulation fans to mix the incoming air and the injected gas.

(a) Helium gas bottles hooked up to all three lines (each row of bottles makes up a line, with lines 2 and 3 running parallel to each other).

(b) PVC valve arrangement showing valve controls for 2 of 3 lines. Each line has three valves, allowing gas to be injected into any sub-stream. The configuration shown is allowing gas from lines 3 and 1 to enter the bottom sub-stream.

Figure 2.3: Gas injection network used for stratification.

To inject fog into the tunnel, two fog machines are located on a shelving tower standing in front of the upstream nozzle, shown in figure 2.4. The High End Systems® F-100™ machine is used for light extinction experiments where a high volume and less precise amount of fog is needed. A Pea Soup® machine is used for PIV experiments, where a precise fog concentration is required in both heavy and light fluid streams, as well as consistent fog particle size.

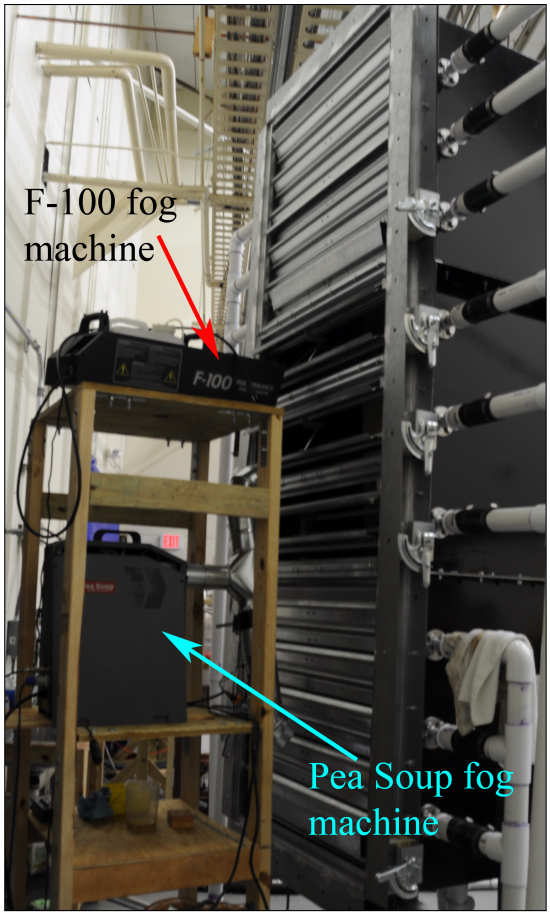

(a) Fog machine tower and flow adjustment louvers at entrace of tunnel, showing both High End F-100^{TM} and Pea Soup® machines.

(b) Louver adjustment control arm used to manipulate the flow velocity through a given sublayer.

Figure 2.4: Velocity and fog control system used to induce shear between streams and inject fog for diagnostics.

Three diagnostic techniques were used to collect data from this facility. They are light extinction using a DSLR camera and back light [shown in figure 2.2(a)], particle-image velocimetry, and hot-wire anemometry. Light extinction experiments are conducted to determine the growth of the mixing layer as the flow moves through the tunnel, whereas PIV and hot-wire diagnostics are used to set the velocities for an experiment. These techniques will be discussed in detail in § 2.2.1 through § 2.2.3.

Additionally, thermocouples are installed in the beginning of the test section to measure the temperature of each respective stream (K-type in the middle stream, E-type in the bottom). It should be noted that since the experiments conducted in this work were only two layer, no thermocouple was installed in the top stream.

Throughout the work presented in this thesis, the facility described above has undergone numerous modifications which are outlined in the appendix. However, the general operating principles have remained the same.

2.2 Experimental Procedure and Configurations

The experiments presented in this work were completed with the light fluid being composed of a mixture of air and helium, and the heavy fluid being pure air. The volume fraction of air to helium in the light mixture sets the Atwood number of the experiment. The bulk velocity within the tunnel is controlled by the fan, located at the exit of the tunnel. It is operated by a control box, pictured in figure 2.5, which allows the fan to be powered on as well as the interior blade angle of attack to be adjusted. Since this particular fan does not utilize a variable frequency drive, the velocity in the tunnel can only be changed by manipulating these blades, opening or closing the upstream louvers, or adjusting the position of the fan (moving it closer/further from the final contraction section). Coarse velocity adjustment is accomplished through fan modifications, while fine adjustment (such as modifying shear during an experiment) is accomplished through louver manipulation.

Figure 2.5: Power box used to operate fan and blade angles. The large white dial displays the pitch angle of the blades, which ensures consistency between experiments.

Once the fan is running steadily, the velocities are set to their specific value for a given experiment. To do this, hot-wire anemometry and PIV are used. When the desired tunnel conditions are verified, gas is injected using the system described in § 2.1. The three different diagnostic techniques used for data collection during experiments are discussed in detail in the following subsections.

2.2.1 Light Extinction

To conduct light extinction experiments, fog is injected into either the light or heavy stream using the High End Systems F-100$^{\text{TM}}$ fog generator. The test section is then illuminated using a backlight composed of eight LED panels. As the fogged and non-fogged streams mix due to instability growth, the fog becomes less concentrated in the mixing region and therefore allows more light to pass through to the camera, as described by the Beer–Lambert law,

$$I = I_0 \, e^{-\mu x} \tag{2.1}$$

where I is the power of the transmitted light, I_0 is the power of the light source, μ is the attenuation coefficient, and x is the path length. For low levels of fog, the transmission power of light through a medium follows a linear relationship with the fog concentration and the attenuation. The purpose of the calibration is to determine the correct amount of fog so that this linear relationship is satisfied.

Calibration experiments are conducted using a triangular prism that is filled with fog, as done by [56]. The triangular cross section produces a linear fog concentration in a given direction. This calibration is shown in figure 2.6.

Figure 2.6: Triangular prism inside test section used for calibration of concentration curves with backlight. Image taken using Nikon® D90™ camera. Fog concentration increases linearly from right to left inside the prism.

Light extinction experiments are conducted using a Nikon® D90™ DSLR camera mounted to a tripod, which is then automated by a LabVIEW™ program to take images at 2 Hz for 100 seconds. These images are then processed using MATLAB®.

An example of a processed instantaneous image and the result of image averaging is given in figure 2.7.

(a) Corrected instantaneous experimental image for Atwood number 0.055 with $\Delta U = 0.16\ m/s$. The characteristic Rayleigh–Taylor plume structures are clearly visible.

(b) Average image after processing for Atwood number 0.055 and $\Delta U = 0.16\ m/s$. Image has been averaged over 100 images similar to the one shown above in figure 2.7(a).

Figure 2.7: Instantaneous and averaged images shown after MATLAB® processing for an experiment with Atwood number 0.055 and $\Delta U = 0.16\ m/s$.

This processing provides the mixing width, growth rate parameter, concentration profiles, and the locations of the mixing width center and the transition region. Additionally, these experiments allow visual verification that the tunnel is operating as expected for the given setup. Light extinction experiments are used to measure

the growth of the mixing layer. From the mixing layer data, the non-dimensional growth parameter $\alpha_{b,s}$ and the height gradient plots are obtained.

2.2.2 Particle-Image Velocimetry

Particle image velocimetry uses TSI® model 630157 PowerView Plus™ 2 megapixel cameras and a dual head Litron® Nano-PIV™ model LPU550 laser with optical arrangement to make measurements in the flow field. Using the Pea Soup® fog machine, particles are introduced into the light and heavy streams. For PIV, particles are seeded in both the heavy and light fluid streams. Seeding is controlled using a duct network with internal fans that splits the fog into two streams. The power of the internal fans is adjusted using a variable transformer. If a larger number of particles is needed in a given stream, the power of the fan can be increased, or the power of the other fan can be reduced. This setup is shown in figure 2.8, and allows a precise, consistent, and steady fog stream to be produced.

Figure 2.8: Variable transformers used for controlling internal fans in the fog splitting system. The voltage controls the fan power, and the seeding for the given stream during PIV experiments.

To illuminate the fog particles, the Litron® laser is used to generate a plane parallel to the z-axis into the test section [shown in figure 2.9(c)]. Two cameras are used at two x locations and are triggered simultaneously. To accomplish this two-location setup while only using one laser, the beam must be split using a beam splitter. This reflects 45% of the power in a specified direction, while allowing 55% of the power to pass through. The 55% beam then travels through a 12.7 mm plano-concave lens which causes the beam to diverge in a plane. This plane is then reflected into the test section. A similar setup is used with the 45% beam at a different x location in the test section. The optical setup is shown in figure 2.9.

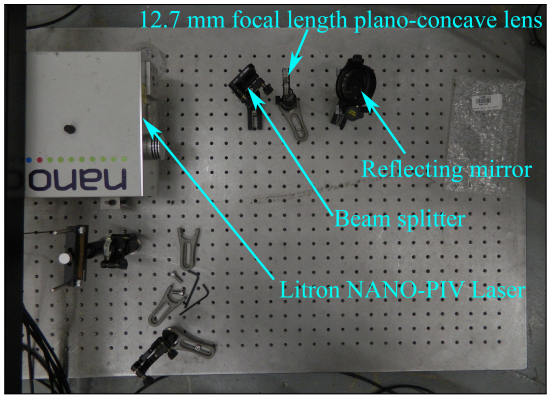

(a) Primary laser table (downstream location). The laser fires the beam which is then split in the beam splitter (45/55% power). The beam then passes through a diverging plano-concave lens before being reflected through the bottom of the test section.

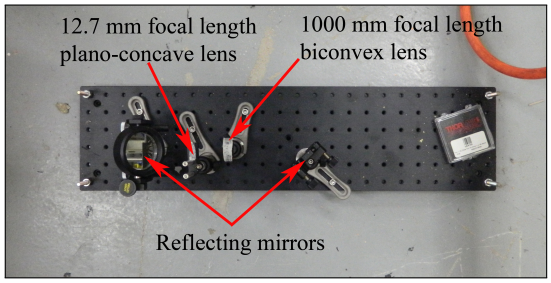

(b) Secondary laser table (upstream location). The laser beam hits the first reflecting mirror (right) after being split in the beam splitter, and then passes through two lenses before being reflected into the channel by the second reflecting mirror (left).

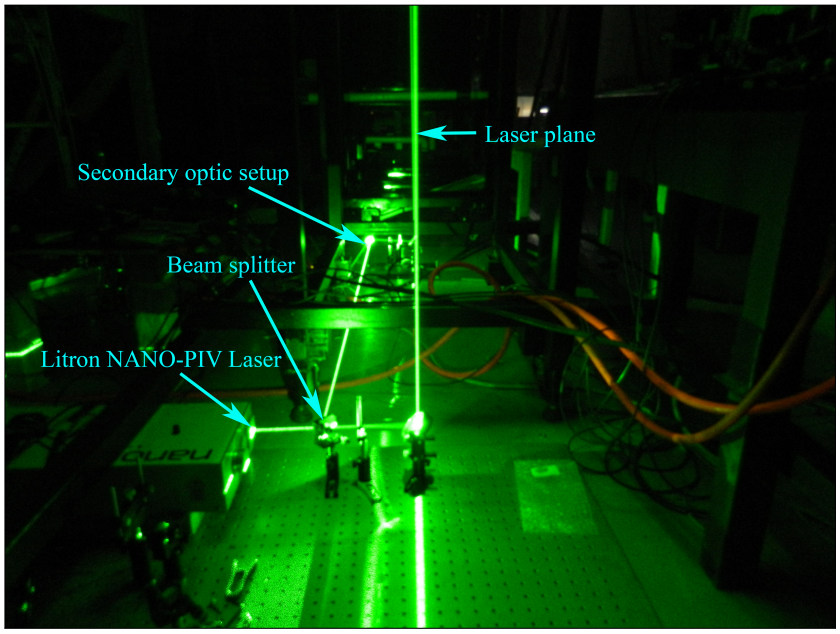

(c) Laser during PIV experiment, showing beam being split in beam splitter, and laser plane being reflected into the test section.

Figure 2.9: Laser table optical arrangements at both stream-wise locations and during an experiment.

The Litron® laser is a dual head laser, which discharges light from each head with a known time interval between discharges. When each laser head is fired, the cameras take a picture: this results in two images at two different times for each camera. A calibration image is then taken: this creates a conversion between pixels and a length scale. These images are then processed using Insight4G™ software from TSI®. The velocity is obtained by using the calibration image to calculate the distance the particle has traveled and the time between images. This process is repeated for the duration of the experiment, and the data is again averaged over the total time.

A sample PIV image taken during a shear experiment is given in figure 2.10. In this image, the seeding is more dense in the top stream, allowing the large vortical structure to appear. After processing with Tecplot®, the vorticity field is obtained. As expected, there is large positive vorticity at the center of the vortex, validating the PIV technique.

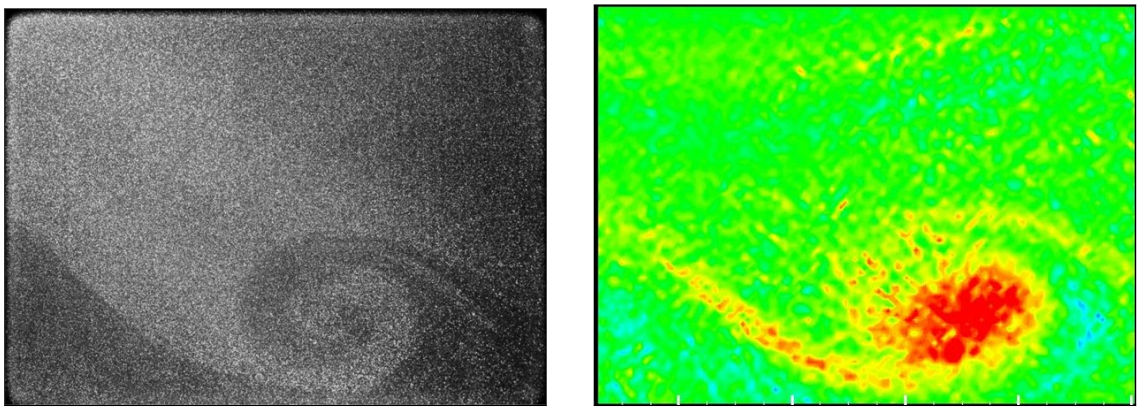

(a) Sample PIV image taken during shear experiment with $\Delta U = 0.06\ m/s$ and $U_m = 0.66\ m/s$.

(b) Vorticity plot showing large positive vorticity at the center of the vortex.

Figure 2.10: Sample experimental PIV image with analysis, showing good agreement between raw image and post-processing.

In order to acquire more data per experiment, two cameras are used simultaneously. This allows data to be collected at two locations downstream of the splitter plate. This diagnostic also allows the turbulent correlations $\overline{u'^2}$, $\overline{v'^2}$, $\overline{u'v'}$ to be calculated. The PIV diagnostic was used for setting the velocities in order to ensure the correct shear value for a given experiment.

2.2.3 Hot and Cold-Wire Anemometry

The third diagnostic technique used in the gas tunnel is hot/cold-wire anemometry with a density probe. Hot-wire, or constant-temperature anemometry (CTA), operates by keeping an extremely thin wire at a constant temperature. Through convective heat transfer, the wire will be cooled as a flow passes over it. The wire must then be heated by increasing the voltage. As the flow velocity increases, the voltage must further be increased to keep up with the wire cooling. Thus, a relationship between voltage and flow velocity can be obtained. Cold-wire, or constant-current anemometry (CCA), operates in a similar fashion except the wire is kept at a constant current rather than temperature. This allows the temperature of the flow to be measured, which is necessary to apply the appropriate correction factor to the velocity and density data.

The hot/cold-wire with density probe configuration requires a three-wire hot-wire probe to measure velocity data in the x, y, and z coordinates, a cold wire to measure the temperature of the flow, and a x-probe to measure the concentration of the mixing fluids. The probes in their experimental configuration are shown in figure 2.11, along with a scale to show the spatial resolution.

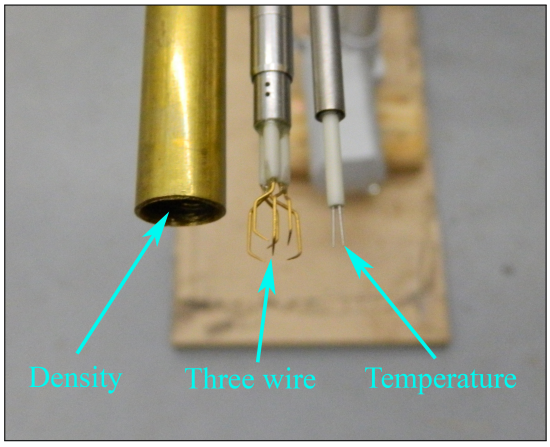

(a) Probe arrangement used for setting velocity and measuring the density profile in the bottom stream.

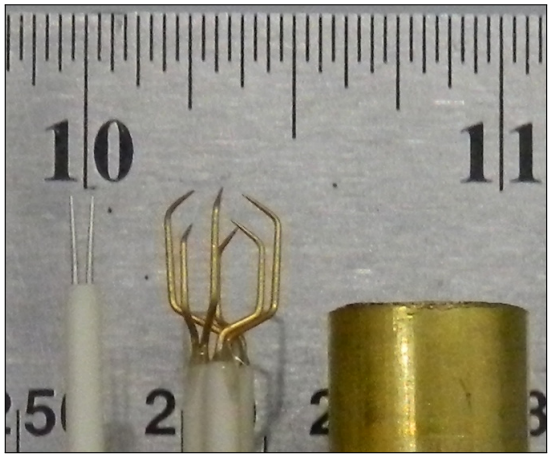

(b) Arrangement with scale to show spatial resolution of probes.

Figure 2.11: Experimental hot-wire arrangement.

The output signal from the anemometers is given as a voltage, and thus, a calibration is required to extract flow properties. This is completed by creating a known mixture of gases with a known velocity in a calibration chamber as shown in figure 2.12.

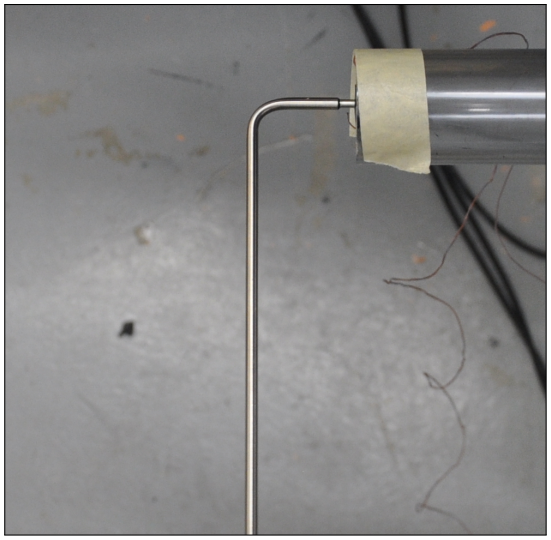

(a) Three wire x-probe. This probe was not used in the experiments presented in this work, but is shown to demonstrate the calibration of a probe.

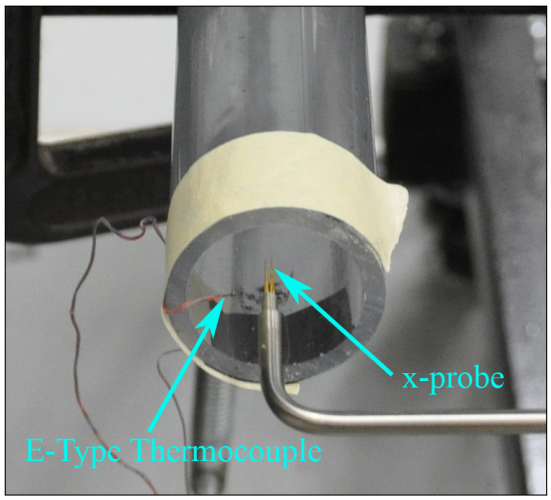

(b) Probe inside calibration chamber with thermocouple. The thermocouple is necessary for temperature corrections to ensure proper readings from the probe.

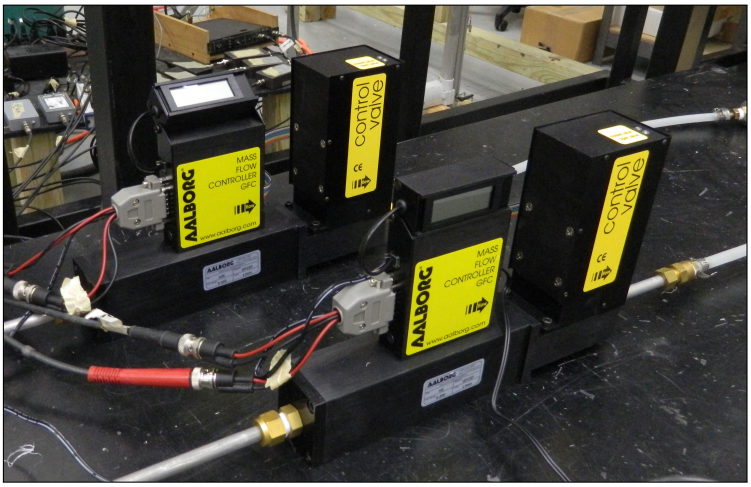

(c) AALBORG® model GFC57 flow controllers which are controlled by a LabVIEW™ program. Flow controllers allow the calibration to be automated, reducing the time required for calibration.

Figure 2.12: Calibration of x-probe hot wire.

For a complete calibration, the voltages must be measured for all conditions in the experiment: this means concentrations from pure air to pure helium (for very high Atwood numbers), and velocities from zero to the maximum experimental velocity. Anytime a probe breaks or if the resistance of the BNC wire changes (due to faulty connections) the probe must be re-calibrated. This can be difficult to detect, and so calibrations are performed each day that an experiment is to be performed.

Gas concentrations and flow rates are regulated using two AALBORG® model GFC57 flow controllers through LabVIEW™. Calibration curves are then generated using King's law,

$$E^2 = A + Bu^c \tag{2.2}$$

where E is output voltage, u is velocity, and A, B, and exponent c are constants calculated during calibration. By using the calibration curves, the output voltages obtained during an experiment are converted into fluid velocity. A detailed description of hot-wire anemometry is given by Banerjee [56]. The hot-wire diagnostics are used in conjunction with PIV to determine that the velocities are correct for the experiments. PIV is used first, and then confirmed with the hot wires. The density probe is used to measure the profile in the bottom stream, which is used to set the initial condition of the simulations, and will be discussed in section 4.

3. REYNOLDS–AVERAGED NAVIER–STOKES CODE

The model used to simulate the experiments in this work is a multicomponent K–ε RANS model originally developed by Dr. Oleg Schilling at Lawrence Livermore National Laboratory and previously used to simulate the Richtmyer–Meshkov instability with reshock [57, 58]. An extensive description of the RANS methodology is given by Pope [59]. The code was further developed by the Author and lab mate Bhanesh Akula in collaboration with Dr. Schilling. This section will describe the numerical methods, governing equations solved by the code, and the initial conditions with the problem setup.

3.1 Numerical Methods

In the earlier Richtmyer–Meshkov simulations performed by Morán-López and Schilling, [57, 58], shock waves are present. Thus, the weighted essentially non-oscillatory (WENO) scheme is used to capture discontinuities within the domain. The governing equations are then implemented with advective flux reconstruction, and time discretization is performed with a third-order total variation diminishing (TVD) Runge–Kutta method. A detailed discussion of the WENO scheme and TVD Runge–Kutta time discretization is given by Liu *et al.* [60]. Additionally, a description of the numerical methods used in the explicit time evolution scheme is given by Morán-López and Schilling [57].

Since the Rayleigh–Taylor instability does not have discontinuities in the flow field, a central difference scheme can be used instead of the flux reconstruction. The central differencing scheme uses linear interpolations to determine values at the face of each cell [61]. However, in the results presented, the flux splitting scheme was applied to the advection terms in the governing equations described above in § 3.2,

while central differencing is used to compute the derivatives in the source and sink terms. The implicit Crank–Nicolson formulation has replaced the third-order TVD method for the time evolution.

3.2 Governing Equations

The RANS model describes the transport of the mean density $\overline{\rho}$, and mean velocity $\tilde{v}$, mean total energy $\tilde{e}$, and the mean heavy mass fraction $\widetilde{m}_H$, where the over bar and tilde signifies a Reynolds average and Favre average, respectively. The code solves seven equations corresponding to the conservation of mass, momentum, total energy, heavy mass fraction, turbulent kinetic energy, turbulent kinetic energy dissipation rate, and density variance. These equations are given below [58]. Since the code is one-dimensional, indices have been omitted.

3.2.1 Explicit Model Equations

Equations for the mean density and momentum are given as

$$\frac{\partial \overline{\rho}}{\partial t} + \frac{\partial}{\partial x}(\overline{\rho}\,\tilde{v}) = 0 \tag{3.1}$$

and

$$\frac{\partial}{\partial t}(\overline{\rho}\,\tilde{v}) + \frac{\partial}{\partial x}(\overline{\rho}\,\tilde{v}^2) = \overline{\rho}\,g - \frac{\partial \overline{p}}{\partial x} - \frac{\partial \tau}{\partial x} + \frac{\partial \overline{\sigma}}{\partial x}, \tag{3.2}$$

where $\overline{\rho}$ is the mean density, $\tilde{v}$ is the mean velocity, $\overline{p}$ is the mean pressure, τ is the Reynolds stress, and $\overline{\sigma}$ is the viscous stress,

$$\tau = \frac{2}{3}\,\overline{\rho}\,K - \frac{4}{3}\,\mu_t\,\frac{\partial \tilde{v}}{\partial x} \tag{3.3}$$

$$\overline{\sigma} = \frac{4}{3}\,\overline{\mu}\,\frac{\partial \tilde{v}}{\partial x}\,, \tag{3.4}$$

and g is the acceleration.

The total mean energy equation is then given as

$$\begin{aligned}\frac{\partial}{\partial t}(\overline{\rho}\,\tilde{e}) + \frac{\partial}{\partial x}(\overline{\rho}\,\tilde{e}\,\tilde{v}) = &\overline{\rho}\,g\,\tilde{v} - \frac{\partial}{\partial x}(\overline{p}\,\tilde{v} + \overline{p}\,\overline{v''}) + \frac{\partial}{\partial x}(\overline{\sigma}\,\tilde{v} - \tau\,\tilde{v}) + \frac{\partial \overline{H}}{\partial x} \\ &+ \frac{\partial}{\partial x}\left[(\overline{\kappa} + \kappa_t)\frac{\partial \widetilde{T}}{\partial x} + \frac{\mu_t}{\sigma_U}\frac{\partial \widetilde{U}}{\partial x}\right] \\ &+ \frac{\partial}{\partial x}\left[\left(\overline{\mu} + \frac{\mu_t}{\sigma_K}\right)\frac{\partial K}{\partial x}\right],\end{aligned} \tag{3.5}$$

where $\overline{v''}$ is the averaged Favre fluctuating velocity, $\overline{H}$ is the total mean enthalpy diffusion, $\widetilde{T}$ is the Favre averaged mean temperature, $\overline{\kappa}$ is the thermal conductivity, and $\overline{\mu}$ is the dynamic viscosity. The terms on the right hand side of equation 3.5 represent the gravitational pressure work, turbulent kinetic energy production, enthalpy diffusion, temperature diffusion, mean internal energy diffusion, and turbulent kinetic energy diffusion, respectively (the subscript t denotes a turbulent quantity). The turbulent thermal conductivity and viscosity are

$$\kappa_t = \frac{\overline{c}_p\,\mu_t}{Pr_t}, \tag{3.6}$$

$$\nu_t = \frac{\mu_t}{\overline{\rho}} = C_\mu \frac{K^2}{\varepsilon} \tag{3.7}$$

where K is the turbulent kinetic energy and ε is the turbulent kinetic energy dissipation rate. Additionally the turbulent Prandtl number, Pr_t, is set to 0.7 and the dimensionless model coefficient is $C_\mu = 0.09$. The mean total energy is the sum of the mean kinetic energy, mean internal energy $\widetilde{U}$, and turbulent kinetic energy

$$\tilde{e} = \frac{\tilde{v}^2}{2} + \widetilde{U} + K. \tag{3.8}$$

This code models the fluids as ideal gases with constant specific heats. Thus, the mean internal energy can be written as

$$\widetilde{U} = \frac{\overline{p}}{(\overline{\gamma}-1)\overline{\rho}} = \overline{c}_v \widetilde{T}, \tag{3.9}$$

where $\overline{\gamma}$ is the ratio of specific heats and can be expressed in terms of the heavy (m_H) and light ($1 - m_H$) mass fraction as

$$\overline{\gamma} = \frac{\overline{c}_p}{\overline{c}_v} = \frac{c_{pH}\widetilde{m}_H + c_{pL}(1-\widetilde{m}_H)}{c_{vH}\widetilde{m}_H + c_{vL}(1-\widetilde{m}_H)}, \tag{3.10}$$

where c_p and c_v are the specific heats at constant volume and pressure, and subscripts H and L represent heavy and light fluid mixtures.

The total mean enthalpy diffusion in equation 3.5 is (indices $r, s = 1, 2$ are used to denote fluids H and L respectively)

$$\overline{H} = -\sum_{r=1}^{2} \tilde{h}_r \overline{J}_{r,j} + \tilde{h}_r \overline{J''_{r,j}} + \overline{h''_r J''_{r,j}}. \tag{3.11}$$

The mean enthalpy for an ideal gas r is

$$\tilde{h} = c_{p,r}\widetilde{T} \tag{3.12}$$

where the mean diffusive flux

$$\overline{J}_r = -\overline{\rho}\left(D_r \frac{\partial \widetilde{m}_r}{\partial x} - \widetilde{m}_r \sum_{s=1}^{2} D_s \frac{\partial \widetilde{m}_s}{\partial x} \right). \tag{3.13}$$

Substituting equations 3.13 and 3.12 into equation 3.11 gives

$$\overline{H} = \overline{\rho} \sum_{r=1}^{2} \tilde{h}_r \left(D_r \frac{\partial \widetilde{m}_r}{\partial x} - \widetilde{m}_r \sum_{s=1}^{2} D_s \frac{\partial \widetilde{m}_s}{\partial x} \right) + \overline{\rho} D_t \sum_{r=1}^{2} \tilde{h}_r \frac{\partial \widetilde{m}_r}{\partial x} \tag{3.14}$$

where the turbulent diffusivity is $D_t = \nu_t / Sc_t$, with the turbulent Schmidt number, $Sc_t = 0.7$.

The molecular transport coefficients such as mass diffusivity and thermal conductivity ($\overline{D}$ and $\overline{\kappa}$, respectively) are determined using the binary mixture relation

$$\overline{\phi} = \frac{\frac{\phi_H \widetilde{m}_H}{\sqrt{MW_H}} + \frac{\phi_L (1 - \widetilde{m}_H)}{\sqrt{MW_L}}}{\frac{\widetilde{m}_H}{\sqrt{MW_H}} + \frac{1 - \widetilde{m}_H}{\sqrt{MW_L}}}, \tag{3.15}$$

where MW_H and MW_L denote the molecular weights of the heavy and light mixtures respectively.

The heavy mass fraction is obtained from

$$\frac{\partial}{\partial t}(\overline{\rho}\, \widetilde{m}_H) + \frac{\partial}{\partial x}(\overline{\rho}\, \widetilde{m}_H\, \tilde{v}) = -\frac{\partial \overline{J}_H}{\partial x} + \frac{\partial}{\partial x}\left(\frac{\mu_t}{\sigma_m} \frac{\partial \widetilde{m}_H}{\partial x} \right), \tag{3.16}$$

where $\overline{J}_H$ is the diffusive flux (equation 3.13).

The turbulent equations will now be presented and discussed. In the K–ε model, equations for the turbulent kinetic energy and its dissipation rate are also solved. Beginning with the turbulent kinetic energy equation

$$\begin{aligned} \frac{\partial}{\partial t}(\overline{\rho}\, K) + \frac{\partial}{\partial x}(\overline{\rho}\, K\, \tilde{v}) = & -\overline{v''} \frac{\partial \overline{p}}{\partial x} - \tau \frac{\partial \tilde{v}}{\partial x} - \overline{\rho}\, \varepsilon + \Pi_K \\ & + \frac{\partial}{\partial x}\left[\left(\overline{\mu} + \frac{\mu_t}{\sigma_K} \right) \frac{\partial K}{\partial x} \right], \end{aligned} \tag{3.17}$$

where ε is the turbulent kinetic energy dissipation rate and Π_K is the pressure

dilatation (which is set to zero in the present work)

$$\Pi_K = \overline{p' \frac{\partial v''}{\partial x}} \,. \tag{3.18}$$

The equation for the turbulent kinetic energy dissipation rate is then given as

$$\begin{aligned} \frac{\partial}{\partial t}(\overline{\rho}\,\varepsilon) + \frac{\partial}{\partial x}(\overline{\rho}\,\varepsilon\,\tilde{v}) = &- C_{\varepsilon_0}\frac{\varepsilon}{K}\,\overline{v''}\,\frac{\partial \overline{p}}{\partial x} - C_{\varepsilon_1}\frac{\varepsilon}{K}\,\tau^d\,\frac{\partial \tilde{v}}{\partial x} - \frac{2}{3}\,C_{\varepsilon_3}\,\overline{\rho}\,\varepsilon\,\frac{\partial \tilde{v}}{\partial x} \\ &- C_{\varepsilon_2}\frac{\overline{\rho}\,\varepsilon^2}{K} + C_{\varepsilon_4}\frac{\varepsilon}{K}\,\Pi_K + \frac{\partial}{\partial x}\left[\left(\overline{\mu} + \frac{\mu_t}{\sigma_\varepsilon}\right)\frac{\partial \varepsilon}{\partial x}\right], \end{aligned} \tag{3.19}$$

where the first five terms on the right side are the pressure work, production, divergence, destruction rate, and dilatation. The sixth term represents the diffusion of the turbulent kinetic energy dissipation rate. The Boussinesq closure model is used for the Reynolds stress:

$$\tau = \frac{2}{3}\,\overline{\rho}\,K - \frac{4}{3}\,\mu_t\,\frac{\partial \tilde{v}}{\partial x} \tag{3.20}$$

and the deviatoric part of the Reynolds stress is

$$\tau^d = -\frac{4}{3}\,\mu_t\,\frac{\partial \tilde{v}}{\partial x} \,. \tag{3.21}$$

The averaged Favre fluctuating velocity $\overline{v''}$ is computed using the closure

$$\overline{v''} = -\left(\frac{\nu_t}{\sigma_\rho(\overline{c}_{p_H} - \overline{c}_{p_L})\,m_H\,\overline{c}_{p_L}}\right)\frac{\partial \tilde{s}}{\partial x}, \tag{3.22}$$

where $\tilde{s}$ is the mean entropy.

Finally, the density variance equation, where $S = \overline{\rho'^2}$ is

$$\begin{aligned}\frac{\partial S}{\partial t} + \frac{\partial}{\partial x}(S\,\tilde{v}) =& 2\,\rho\,\overline{v''}\,\frac{\partial \overline{p}}{\partial x} + S\,\frac{\partial \tilde{v}}{\partial x} + \frac{\overline{\rho^2}}{\overline{\gamma}\,\overline{p}}\,\Pi_K - 2\,C_\rho\,S\,\frac{\varepsilon}{K} \\ &+ \frac{\partial}{\partial x}\left[\left(\overline{D} + \frac{\nu_t}{Sc_t\,\sigma_S}\right)\frac{\partial S}{\partial x}\right]\end{aligned} \tag{3.23}$$

can be used as a diagnostic, and allows for more quantities to be obtained such as the molecular mixing parameter, θ. The molecular mixing parameter is a measure of how well mixed the light and heavy fluids are. In equation 3.23, $\overline{D}$ represents the mass diffusivity of the mixture. The terms on the right hand side of equation 3.23 are the production, divergence, dilatation, destruction, and diffusion of the density variance. The density variance is not used in the present work, and is included for completeness.

The dimensionless model coefficients C_{ε_0}, C_{ε_1}, C_{ε_2}, C_{ε_3}, and C_{ε_4} are given in table 3.1 along with σ_ρ, σ_m, σ_U, σ_K, σ_ε, and σ_S. These values were chosen to give a theoretical α of 0.07.

Table 3.1: Model coefficients.

C_{ε_0}	0.90	σ_ρ	0.90
C_{ε_1}	1.44	σ_m	0.70
C_{ε_2}	1.92	σ_U	0.70
C_{ε_3}	0.00	σ_K	0.70
C_{ε_4}	2.00	σ_ε	0.70
		σ_S	0.70

3.3 Code Development

As part of the work for this thesis, the code has been further developed in order to better and more efficiently simulate the experiments conducted in the gas tunnel.

These modifications include adding initial gas mixture capability, implementing a new model for mixture viscosity, including an option for a central differencing scheme for the advection terms, and solving the governing equations using the implicit Crank–Nicolson method.

Too add mixture capability to the code, simple thermodynamic relations were used based on the mole fraction of the mixture. This mole fraction is also used to set the heavy and light fluid density (and consequently Atwood number) of the simulation. This method does not, however, apply for the viscosity of a mixture. For this, an empirical expression has been used from Buddenberg and Wilke [62] to determine the constants in the Sutherland–Thiesen viscosity equation for a binary gas mixture

$$\overline{\mu} = \frac{\mu_1}{1 + \frac{X_2}{X_1}\frac{1.385\mu_1}{D_{12}\rho_1}} + \frac{\mu_2}{1 + \frac{X_1}{X_2}\frac{1.385\mu_2}{D_{12}\rho_2}}, \tag{3.24}$$

where subscripts 1 and 2 denote the components of the binary mixture, and $\mu_{1,2}$, $X_{1,2}$, $D_{1,2}$, and $\rho_{1,2}$ are the viscosity, mole fractions, mass diffusivity, and density of the component fluids.

Finally, in order to simulate the gas tunnel experiments, an implicit time-evolution method was used. The explicit scheme is limited by the Courant–Friedrichs–Lewy (CFL) condition, which is required to ensure stability. The seven equations labeled above in bold will now be given in their implicit form, as used in the Crank–Nicolson scheme. To accomplish this, the equations must first be simplified according to term discretization. The term f_ϕ will be used to represent advection and additional terms (discretized using the WENO or central differencing scheme), while S_ϕ will contain the source/sink terms whose derivatives are discretized using central differencing. Subscript ϕ will be assigned for the appropriate equation.

3.3.1 Implicit Model Equations

Using the mechanism mentioned above, the momentum equation (equation 3.2) can be represented as:

$$\frac{\partial}{\partial t}(\overline{\rho}\,\tilde{v}) = \frac{4}{3}\frac{\partial}{\partial x}\left[(\overline{\mu}+\mu_t)\frac{\partial \tilde{v}}{\partial x}\right] + f_{\tilde{v}} + S_{\tilde{v}}, \tag{3.25}$$

where

$$f_{\tilde{v}} = -\frac{\partial}{\partial x}(\overline{\rho}\tilde{v}^2) - \frac{\partial}{\partial x}(\overline{p}+p_t),$$

$$S_{\tilde{v}} = \overline{\rho}g$$

Implementing equation 3.25 in the Crank–Nicolson formulation results in

$$\begin{aligned}\overline{\rho}_j^{n+1}\frac{\tilde{v}_j^{n+1}-\tilde{v}_j^n}{\Delta t} = &\frac{\frac{4}{3}(\overline{\mu}_{j+\frac{1}{2}}^{n+1}+\mu_{t_{j+\frac{1}{2}}})(\tilde{v}_{j+1}^{n+1}-\tilde{v}_j^{n+1})}{2(\Delta x)^2} \\ &- \frac{\frac{4}{3}(\overline{\mu}_{j-\frac{1}{2}}^{n+1}+\mu_{t_{j-\frac{1}{2}}})(\tilde{v}_j^{n+1}-\tilde{v}_{j-1}^{n+1})}{2(\Delta x)^2} \\ &+ f_{\tilde{v},j}^n + S_{\tilde{v},j}^n,\end{aligned} \tag{3.26}$$

where the exponent n represents the time step and subscript j the index location within the 1D domain. The diffusion coefficients $\overline{\mu}_{j+\frac{1}{2}}$ and $\overline{\mu}_{j-\frac{1}{2}}$ are taken as nodal averages and are defined as

$$\overline{\mu}_{j\pm\frac{1}{2}} = \frac{\overline{\mu}_j + \overline{\mu}_{j\pm1}}{2}. \tag{3.27}$$

Equation 3.27 represents the method used for all diffusion coefficients in the Crank–Nicolson formulation. To solve equation 3.26, terms at the next time step $(n+1)$ are moved to the left hand side of the equation while the current time step

(n) terms are kept on the right. The resulting equation is then written as:

$$\begin{aligned} -D^n_{j+\frac{1}{2}}\tilde{v}^{n+1}_{j+1} + (\psi^{n+1}_j + D^n_{j+\frac{1}{2}} + D^n_{j-\frac{1}{2}})\tilde{v}^{n+1}_j - D^n_{j-\frac{1}{2}}\tilde{v}^{n+1}_{j-1} \\ = 2(\Delta x)^2(f^n_{\tilde{v},j} + S^n_{\tilde{v},j}) + \psi^{n+1}_j \tilde{v}^n_j, \end{aligned} \tag{3.28}$$

where D is the diffusion coefficient, $\overline{\mu}_j + \mu_{t_j}$. The term $\psi_j = 2\overline{\rho}^{n+1}_j(\Delta x)^2/\Delta t$ has been introduced for simplicity. Since equation 3.28 represents a tri-diagonal matrix, it can be solved by using the boundary conditions for $\tilde{v}$ and the well known Thomas algorithm with the condition of $\tilde{v} = 0$ at each boundary.

The pressure work, represented by the first term in equation 3.5, is discretized using the central difference of flux splitting scheme. The other terms can be represented in terms of $\tilde{e}$ by rearranging equations 3.8 and 3.9. Thus, turbulent kinetic energy production is written as

$$\frac{4}{3}\frac{\partial}{\partial x}\left[(\mu + \mu_t)\frac{\partial \tilde{e}}{\partial x}\right] - \frac{4}{3}\frac{\partial}{\partial x}\left[(\mu + \mu_t)\frac{\partial}{\partial x}(K + \tilde{U})\right] \tag{3.29}$$

Enthalpy diffusion (equation 3.12) becomes

$$\tilde{h} = \overline{c}_{p,r}\frac{\widetilde{U}}{\overline{c}_v} \Longrightarrow \tilde{h} = \frac{\overline{c}_{p,r}}{\overline{c}_v}\left(\tilde{e} - K - \frac{\tilde{v}^2}{2}\right) \tag{3.30}$$

and when substituted into equation 3.14 gives

$$\overline{H} = \underbrace{\left(\overline{\rho}\sum_{r=1}^{2}\frac{c_{p,r}}{c_{v,mix}}\left(D_r\frac{\partial \widetilde{m}_r}{\partial x} - \widetilde{m}_r\sum_{s=1}^{2}D_s\frac{\partial \widetilde{m}_s}{\partial x}\right) - \overline{\rho}D_t\sum_{r=1}^{2}\frac{c_{p,r}}{c_{v,mix}}\frac{\partial \widetilde{m}_r}{\partial x}\right)}_{A}\left(e - K - \frac{\tilde{v}^2}{2}\right), \tag{3.31}$$

where the coefficient of $(e - K - \frac{\tilde{v}^2}{2})$ is labeled as A for simplicity and clarity in

equations 3.36, 3.37 and 3.39 below.

The Favre averaged temperature is written as

$$\widetilde{T} = \frac{1}{\overline{c}_v}\left(\tilde{e} - K - \frac{\tilde{v}^2}{2}\right), \tag{3.32}$$

so that the temperature diffusion term becomes

$$\frac{\partial}{\partial x}\left[\frac{\tilde{\kappa} + \kappa_t}{\overline{c}_v}\left(\frac{\partial \tilde{e}}{\partial x} - \frac{\partial K}{\partial x} - \tilde{v}\,\frac{\partial \tilde{v}}{\partial x}\right) - \frac{\tilde{\kappa} + \kappa_t}{\overline{c}_v^2}\,\frac{\partial \overline{c}_v}{\partial x}\,\tilde{U}\right] \tag{3.33}$$

In a similar fashion, the mean internal energy diffusion is written as

$$\frac{\partial}{\partial x}\left(\frac{\mu_t}{\sigma_U}\,\frac{\partial \tilde{e}}{\partial x}\right) - \frac{\partial}{\partial x}\left[\frac{\mu_t}{\sigma_U}\,\frac{\partial}{\partial x}(\tilde{v}^2 + K)\right] \tag{3.34}$$

and the turbulent kinetic energy diffusion

$$\frac{\partial}{\partial x}\left[\left(\frac{\mu_t}{\sigma_K} + \overline{\mu}\right)\frac{\partial \tilde{e}}{\partial x}\right] - \frac{\partial}{\partial x}\left[\left(\frac{\mu_t}{\sigma_K} + \overline{\mu}\right)\frac{\partial}{\partial x}(\tilde{v}^2 + \widetilde{U})\right]. \tag{3.35}$$

Equations 3.29, 3.31, and 3.33 through 3.35 are combined to form the complete energy equation

$$\begin{aligned}\frac{\partial}{\partial t}(\overline{\rho}\,\tilde{e}) + \frac{\partial}{\partial x}(\overline{\rho}\,\tilde{e}\,\tilde{v}) \;&= \overline{\rho}\,g\,\tilde{v} - \frac{\partial}{\partial x}(\overline{p}\,\tilde{v} + \overline{p}\,\overline{v}'') \\ &\quad + \frac{\partial}{\partial x}\left[A\left(\tilde{e} - \frac{\tilde{v}^2}{2} - K\right)\right] \\ &\quad + \frac{4}{3}\frac{\partial}{\partial x}\left[\left(\overline{\mu} + \mu_t\right)\frac{\partial}{\partial x}\left(\tilde{e} - \widetilde{U} - K\right)\right] \\ &\quad + \frac{\partial}{\partial x}\left[\frac{\mu_t}{\sigma_U}\frac{\partial}{\partial x}\left(\tilde{e} - \frac{\tilde{v}^2}{2} - K\right)\right] \\ &\quad + \frac{\partial}{\partial x}\left[\left(\overline{\mu} + \frac{\mu}{\sigma_K}\right)\frac{\partial}{\partial x}\left(\tilde{e} - \frac{\tilde{v}^2}{2} - \widetilde{U}\right)\right] \\ &\quad - \frac{\partial}{\partial x}\left[\frac{\kappa_t + \overline{\kappa}}{\overline{c}_v^2}\frac{\partial \overline{c}_v}{\partial x}\left(\tilde{e} - \frac{\tilde{v}^2}{2} + K\right)\right].\end{aligned} \tag{3.36}$$

Equation 3.36 is then reduced as done before, into terms discretized by central difference or flux splitting and terms discretized with the Crank–Nicolson method. This is shown below, with $S_{\tilde{e}}$ representing source terms lagged by one time step.

$$\begin{aligned}\frac{\partial}{\partial t}(\overline{\rho}\,\tilde{e}) =& \frac{\partial}{\partial x}\underbrace{\left[\frac{\kappa + \kappa_t}{\overline{c}_v} + \frac{\mu_t}{\sigma_U} + \overline{\mu} + \frac{\mu_t}{\sigma_K} + \frac{4}{3}(\mu + \mu_t)\right]}_{D^e}\frac{\partial \tilde{e}}{\partial x} + \frac{\partial}{\partial x}(B\,\tilde{e}) \\ &+ f_{\tilde{e}} + S_{\tilde{e}}\end{aligned} \tag{3.37}$$

with the new coefficient

$$B = A - \frac{\overline{\kappa} + \overline{\kappa_t}}{\overline{c}_v^2}\frac{\partial \overline{c}_v}{\partial x},$$

and

$$f_{\tilde{e}} = -\frac{\partial}{\partial x}(\overline{\rho}\,\tilde{e}\,\tilde{v}) - \frac{\partial}{\partial x}(\overline{p}\,\tilde{v} + p_t\,\tilde{v})$$

$$
\begin{aligned}
S_{\tilde{e}} =& \overline{\rho}\, g\, \tilde{v} - \frac{\partial}{\partial x}(\overline{\rho}\,\overline{v''}) - \frac{\partial}{\partial x}\left[A\left(\frac{\tilde{v}^2}{2}+K\right)\right] \\
&- \frac{4}{3}\frac{\partial}{\partial x}\left[(\overline{\mu}+\mu_t)\frac{\partial}{\partial x}\left(\widetilde{U}+K\right)\right] \\
&- \frac{\partial}{\partial x}\left[\frac{\mu_t}{\sigma_U}\frac{\partial}{\partial x}\left(\frac{\tilde{v}^2}{2}+K\right)\right] \\
&- \frac{\partial}{\partial x}\left[\left(\overline{\mu}+\frac{\mu_t}{\sigma_K}\right)\frac{\partial}{\partial x}\left(\frac{\tilde{v}^2}{2}+\widetilde{U}\right)\right] \\
&- \frac{\partial}{\partial x}\left[(\overline{\kappa}+\kappa_t)\frac{\partial}{\partial x}\left(\frac{\tilde{v}^2+2K}{2\,\overline{c}_v}\right)\right].
\end{aligned}
$$

Using equation 3.37, the energy equation can be arranged in the Crank–Nicolson discretization. The term labeled as D^e represents the diffusion coefficient for the energy equation in the Crank–Nicolson discretization

$$
\begin{aligned}
\overline{\rho}_j^{n+1}\frac{\tilde{e}_j^{n+1}-\tilde{e}_j^n}{\Delta t} =& \frac{D^{e,n}_{j+\frac{1}{2}}(\tilde{e}_{j+1}^{n+1}-\tilde{e}_j^{n+1}+\tilde{e}_{j+1}^n-\tilde{e}_j^n)}{2(\Delta x)^2} \\
&- \frac{D^{e,n}_{j-\frac{1}{2}}(\tilde{e}_j^{n+1}-\tilde{e}_{j-1}^{n+1}+\tilde{e}_j^n-\tilde{e}_{j-1}^n)}{2(\Delta x)^2} \\
&+ \frac{B^n_{j+\frac{1}{2}}(\tilde{e}_{j+1}^{n+1}-\tilde{e}_j^{n+1}+\tilde{e}_{j+1}^n-\tilde{e}_j^n)}{2\Delta x} \\
&- \frac{B^n_{j-\frac{1}{2}}(\tilde{e}_j^{n+1}-\tilde{e}_{j-1}^{n+1}+\tilde{e}_j^n-\tilde{e}_{j-1}^n)}{2\Delta x} \\
&+ f^n_{\tilde{e},j} + S^n_{\tilde{e},j},
\end{aligned}
\tag{3.38}
$$

and in the tridiagonal formulation

$$
\begin{aligned}
(-D^{e,n+1}_{j+\frac{1}{2}} - B^{n+1}_{j+\frac{1}{2}}\Delta x)\tilde{e}_{j+1}^{n+1} &+ (\psi_j^{n+1} + D^{e,n+1}_{j+\frac{1}{2}} + D^{e,n+1}_{j-\frac{1}{2}})\tilde{e}_j^{n+1} - (D^{e,n+1}_{j-\frac{1}{2}} + B^{n+1}_{j-\frac{1}{2}}\Delta x)\tilde{e}_{j-1}^{n+1} \\
&= 2(\Delta x)^2(f^n_{\tilde{e},j} + S^n_{\tilde{e},j}) + (D^{e,n}_{j-\frac{1}{2}} + B^n_{j-\frac{1}{2}}\Delta x)\tilde{e}_{j-1}^n \\
&\quad - (D^{e,n}_{j-\frac{1}{2}} + B^n_{j-\frac{1}{2}}\Delta x - \psi_j^{n+1} + D^{e,n}_{j+\frac{1}{2}} + B^n_{j+\frac{1}{2}}\Delta x)\tilde{e}_j^n \\
&\quad + (D^{e,n}_{j+\frac{1}{2}} + B^n_{j+\frac{1}{2}}\Delta x)\tilde{e}_{i+1}^n.
\end{aligned}
\tag{3.39}
$$

In the heavy mass fraction equation, the diffusive flux is discretized using central differencing or flux splitting, and therefore the second term in equation 3.16 must be discretized using the Crank–Nicolson scheme. Equation 3.16 reduces to

$$\frac{\partial}{\partial t}(\rho\widetilde{m}_H) = \frac{\partial}{\partial x}\left(\frac{\mu_t}{\sigma_m}\frac{\partial\widetilde{m}_H}{\partial x}\right) + f_{\widetilde{m}_H} + S_{\widetilde{m}_H} \tag{3.40}$$

with

$$f_{\widetilde{m}_H} = -\frac{\partial}{\partial x}(\overline{\rho}\widetilde{m}_H\tilde{v}),$$

$$S_{\widetilde{m}_H} = -\frac{\partial\overline{J}_H}{\partial x}$$

transforming equation 3.40 into the Crank–Nicolson formulation results in

$$\begin{aligned}\overline{\rho}_j^{n+1}\frac{\widetilde{m}_{H_j}^{n+1} - \widetilde{m}_{H_j}^{n}}{\Delta t} =& \frac{\mu_{t_{j+\frac{1}{2}}}^{n+1}(\widetilde{m}_{H_{j+1}}^{n+1} - \widetilde{m}_{H_j}^{n+1})}{\sigma_m 2(\Delta x)^2} \\ &- \frac{\mu_{t_{j-\frac{1}{2}}}^{n+1}(\widetilde{m}_{H_j}^{n+1} - \widetilde{m}_{H_{j-1}}^{n+1})}{\sigma_m 2(\Delta x)^2} + f_{\widetilde{m}_H,j}^{n} + S_{\widetilde{m}_H,j}^{n}.\end{aligned} \tag{3.41}$$

The diffusion coefficients μ_t/σ_m are defined in a similar fashion to equation 3.27 and represented as D

$$\begin{aligned}-D_{j+\frac{1}{2}}^{n}\widetilde{m}_{H_{j+1}}^{n+1} + (\psi_j^{n+1} + D_{j+\frac{1}{2}}^{n} + D_{j-\frac{1}{2}}^{n})\widetilde{m}_{H_j}^{n+1} - D_{j-\frac{1}{2}}^{n}\widetilde{m}_{H_{j-1}}^{n+1} \\ = 2(\Delta x)^2(f_{\widetilde{m}_H,j}^{n} + S_{\widetilde{m}_H,j}^{n}) + \psi_j^{n+1}\widetilde{m}_{H,j}^{n}.\end{aligned} \tag{3.42}$$

In the turbulent kinetic energy equation (equation 3.17), the turbulent kinetic energy production work, production, destruction rate, and dilation are source terms, which are lagged by one time step. Thus, equation 3.17 can be reduced to

$$\frac{\partial}{\partial t}(\overline{\rho}K) = \frac{\partial}{\partial x}\left[\left(\overline{\mu} + \frac{\mu_t}{\sigma_K}\right)\frac{\partial K}{\partial x}\right] + f_K + S_K, \tag{3.43}$$

which in the Crank–Nicolson formulation is

$$\begin{aligned}\overline{\rho}_j^{n+1}\frac{K_j^{n+1}-K_j^n}{\Delta t} = &\frac{(\overline{\mu}_{j+\frac{1}{2}}+\frac{\mu_{t_{j+\frac{1}{2}}}}{\sigma_K})(K_{j+1}^{n+1}-K_j^{n+1})}{2(\Delta x)^2}\\ &-\frac{(\overline{\mu}_{j-\frac{1}{2}}+\frac{\mu_{t_{j-\frac{1}{2}}}}{\sigma_K})(K_j^{n+1}-K_{j-1}^{n+1})}{2(\Delta x)^2}+f_K^n+S_K^n\end{aligned} \tag{3.44}$$

where

$$f_K = -\frac{\partial}{\partial x}(\overline{\rho}\,K\tilde{v})$$

$$S_K = -\overline{v''}\,\frac{\partial \overline{p}}{\partial x}-\tau\,\frac{\partial \tilde{v}}{\partial x}-\overline{\rho}\,\varepsilon+\Pi_K,$$

In the turbulent kinetic energy equation the diffusion coefficients are $\overline{\mu}_{j\pm\frac{1}{2}}+\mu_{t_{j\pm\frac{1}{2}}}/\sigma_K$ which are again represented as D in

$$\begin{aligned}-D_{j+\frac{1}{2}}^n K_{j+1}^{n+1}+(\psi_j^{n+1}+D_{j+\frac{1}{2}}^n+D_{j-\frac{1}{2}}^n)K_j^{n+1}-D_{j-\frac{1}{2}}^n K_{H_j-1}^{n+1}&\\ =2(\Delta x)^2(f_{K,j}^n+S_{K,j}^n)+\psi_j^{n+1}K_j^n&\end{aligned} \tag{3.45}$$

The ε equation is formulated in a similar way to the K equation, where only the diffusion term is discretized in the Crank–Nicolson formulation. The reduced version of equation 3.19 is written as

$$\frac{\partial}{\partial t}(\overline{\rho}\,\varepsilon)=\frac{\partial}{\partial x}\left[\left(\overline{\mu}+\frac{\mu_t}{\sigma_\varepsilon}\right)\frac{\partial \varepsilon}{\partial x}\right]+f_\varepsilon+S_\varepsilon, \tag{3.46}$$

with

$$f_\varepsilon = -\frac{\partial}{\partial x}(\overline{\rho}\,\varepsilon\,\tilde{v}),$$

and

$$s_\varepsilon = -C_{\varepsilon 0}\,\frac{\varepsilon}{K}\,\overline{v''}\,\frac{\partial \overline{p}}{\partial x}-C_{\varepsilon 1}\,\frac{\varepsilon}{K}\,\tau\,\frac{\partial \tilde{v}}{\partial x}-\frac{2}{3}\,C_{\varepsilon 3}\,\overline{\rho}\,\varepsilon\,\frac{\partial \tilde{v}}{\partial x}-C_{\varepsilon 2}\,\frac{\overline{\rho}\,\varepsilon^2}{K}+C_{\varepsilon 4}\,\frac{\varepsilon}{K}\,\Pi_K.$$

The resulting Crank–Nicolson formulation and discretization (equations 3.47 and 3.48, respectively) is

$$\begin{aligned}\rho_j^{n+1}\frac{\varepsilon_j^{n+1}-\varepsilon_j^n}{\Delta t} =& \frac{(\overline{\mu}_{j+\frac{1}{2}}+\frac{\mu_{t_{j+\frac{1}{2}}}}{\sigma_\varepsilon})(\varepsilon_{j+1}^{n+1}-\varepsilon_j^{n+1})}{2(\Delta x)^2} \\ & - \frac{(\overline{\mu}_{j-\frac{1}{2}}+\frac{\mu_{t_{j-\frac{1}{2}}}}{\sigma_\varepsilon})(\varepsilon_j^{n+1}-\varepsilon_{j-1}^{n+1})}{2(\Delta x)^2} \\ & + f_\varepsilon + S_\varepsilon\end{aligned} \tag{3.47}$$

$$\begin{aligned}-D_{j+\frac{1}{2}}^n\varepsilon_{j+1}^{n+1} + (\psi_j^{n+1}+D_{j+\frac{1}{2}}^n+D_{j-\frac{1}{2}}^n)\varepsilon_j^{n+1} - D_{j-\frac{1}{2}}^n\varepsilon_{j-1}^{n+1} \\ = 2(\Delta x)^2(f_{\varepsilon,j}^n+S_{\varepsilon,j}^n)+\psi_j^{n+1}\varepsilon_j^n\end{aligned} \tag{3.48}$$

Finally, the density variance equation is discretized with the Crank–Nicolson scheme, as as before in § 3.2, $S=\overline{\rho'^2}$. This reduces equation 3.23 to

$$\frac{\partial}{\partial t}(S) = \frac{\partial}{\partial x}\left[\left(\overline{D}+\frac{\nu_t}{Sc_t\sigma_S}\right)\frac{\partial S}{\partial x}\right] + f_S + S_S. \tag{3.49}$$

with

$$f_S = -\frac{\partial}{\partial x}(S\tilde{v}),$$

and

$$S_S = 2\,\overline{\rho}\,\overline{v''}\,\frac{\partial\overline{\rho}}{\partial x} + S\,\frac{\partial\tilde{v}}{\partial x} + 2\,\frac{\overline{\rho}^2}{\overline{\gamma}\,\overline{p}}\,\Pi_K - 2\,C_\rho\,\frac{\varepsilon}{K}\,S.$$

The Crank–Nicolson formulation and discretization is then

$$\begin{aligned}\frac{S_j^{n+1}-S_j^n}{\Delta t} =& \frac{(\overline{D}_{j+\frac{1}{2}}^n+\frac{\nu_{t_{j+\frac{1}{2}}}^{n+1}}{Sc_t\sigma_S})(S_{j+1}^{n+1}-S_j^{n+1})}{2(\Delta x)^2} \\ & - \frac{(\overline{D}_{j+\frac{1}{2}}^n+\frac{\nu_{t_{j+\frac{1}{2}}}^{n+1}}{Sc_t\sigma_S})(S_j^{n+1}-S_{j-1}^{n+1})}{2(\Delta x)^2} + f_{S,i}^n + S_{S,i}^n.\end{aligned} \tag{3.50}$$

The term $D_{j+\frac{1}{2}}$ in equation 3.50 represents the mass diffusivity of the mixture. To avoid confusion in the Crank–Nicolson discretization for the density variance, the diffusion coefficient is represented by Λ,

$$\begin{aligned} -\Lambda^n_{j+\frac{1}{2}} S^{n+1}_{j+1} + (\frac{\psi^{n+1}_j}{\rho^{n+1}_j} + \Lambda^n_{j+\frac{1}{2}} + \Lambda^n_{j-\frac{1}{2}}) S^{n+1}_j - \Lambda^n_{j-\frac{1}{2}} S^{n+1}_{j-1} \\ = 2(\Delta x)^2 (f^n_{S,j} + S^n_{S,j}) + \frac{\psi^{n+1}_j}{\rho^{n+1}_j} S^n_j \end{aligned} \tag{3.51}$$

4. INITIAL CONDITIONS AND PROBLEM SETUPS

In order to complete the objectives outlined in section 1, a total of six cases of experiments were created. Table 4.1 summarizes these experiments by giving the Atwood number, velocity difference, and whether or not the case has complex stratification. A complex stratified flow refers to when the density profile in the light fluid is non-constant. For the experiments performed in this work, this means that the density of the fluid increases with the distance below the splitter plate. If the density profile is constant, it is referred to as generic stratification.

Table 4.1: Experimental summary.

Case	$\boldsymbol{A_t}$	$\boldsymbol{\Delta U}$	**Complex Stratification**
I(a)	0.055	0.16	YES
I(b)	0.055	0.39	YES
I(c)	0.055	0.75	YES
II(a)	0.0971	0.25	YES
II(b)	0.0971	0.94	YES
III(a)	0.147	0.27	YES
III(b)	0.172	1.0	YES
IV	0.07	–	NO
V	0.132	–	NO
VI	0.164	–	NO

4.1 Objective 1

The first objective in § 1.3.1 is to build upon the work by Akula *et al.* [6] and to examine whether or not the transitional Richardson number collapses to the range of -1.5 to -2.5 for higher Atwood numbers. To accomplish this goal, cases I, II, and III will be used. For each of these cases, the Atwood number remains

constant [except III(a) and III(b), which will be discussed later], and the velocity ratio between the streams is changed. By measuring the mixing layer width, the gradient of the bubble height (dh_b/dx) can be calculated (the bubble height is used since the bubbles penetrate into the higher velocity flow). The gradient is taken with respect to downstream tunnel position (x), and plotted against time, where $t = x/U_m$. From the gradient plot, the transition point is located by visual inspection. This occurs where the gradient transitions from a constant value to linear growth, which indicates the mixing layer transitioning from linear to quadratic growth, or Kelvin–Helmholtz mixing to Rayleigh–Taylor mixing. The total mixing width at this point is then used in equation 1.7 to determine the transitional Richardson number.

4.2 Objective 2

The second objective discussed in section 1 is to provide experimental data to quantify the effect of a complex stratified flow, using the mixing layer and non-dimensional growth parameter $\alpha_{b,s}$ for comparison with a generic stratification case. This objective will be completed by comparing Cases I(a), II(a), III(a) with IV, V, and VI. To create the complex stratification [Cases I(a), II(a), and III(a)], pure helium was injected into the tunnel through the pipe network. This causes pockets of helium to rise up to the splitter plate, resulting in a non-constant density profile, referred to as complex stratification. For the generic stratification (Cases IV, V, VI), nitrogen was installed on one of the vacant gas lines. This allowed mixing to occur inside the pipe network, resulting in a mixture being injected into the tunnel and creating a constant density profile (referred to as generic stratification). Figures are provided below showing the profiles.

For Case I, the average experimental Atwood number was set at 0.055 using one helium line (a total of six bottles) and an orifice of diameter 0.072" (0.183 cm). As this was the lowest Atwood number, and therefore smallest amount of injected helium, it was expected that this case should have the highest density variation in the light fluid stream. With low volumes of helium, the fluid becomes more difficult to mix, resulting in high concentrations of helium directly below the splitter plate, and high concentrations of air near the bottom of the stream. This was confirmed with the density probe, with the results shown in figure 4.1. For Case IV, nitrogen bottles were used with a 0.110" (0.279 cm) diameter orifice in conjunction with the helium line using the 0.072" (0.183 cm) orifice.

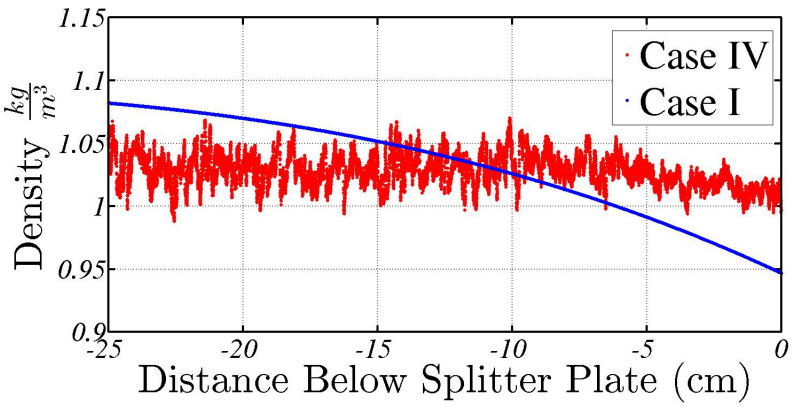

Figure 4.1: Profiles obtained with the density x-probe for Cases I and IV.

In Case II, two helium lines were used with orifices of 0.072" (0.183 cm) and 0.084" (0.213 cm). This resulted in an average Atwood number of 0.0971. The density profile is flatter in Case II than in Case I. For Case V, nitrogen was injected using the third vacant gas line and an orifice of diameter 0.185" (0.470 cm), and the density profile is shown in figure 4.2. This orifice was the largest available, and was required

since the helium injection was much higher than in Case II.

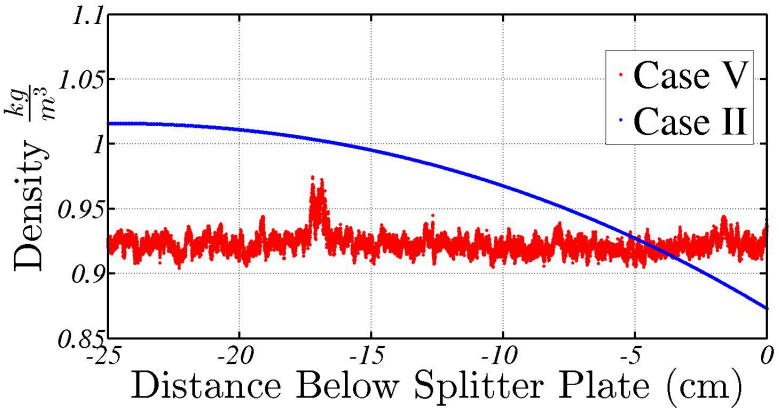

Figure 4.2: Profiles obtained with the density x-probe for Cases II and V.

Finally in Case III, the average Atwood number reached its largest value. Helium was again injected from two lines, with orifices of sizes 0.072" (0.183 cm) and 0.110" (0.279 cm) which resulted in $A_t = 0.147$. For Case III(b), the Atwood number is slightly higher due to the velocity of the bottom stream being set lower between experiments. The lower velocity (less air entering the tunnel) effectively reduces the dilution of the helium by increasing its concentration inside the tunnel. Again, the 0.185" (0.470 cm) orifice was used for nitrogen injection in Case VI, and the density profiles are given in figure 4.3.

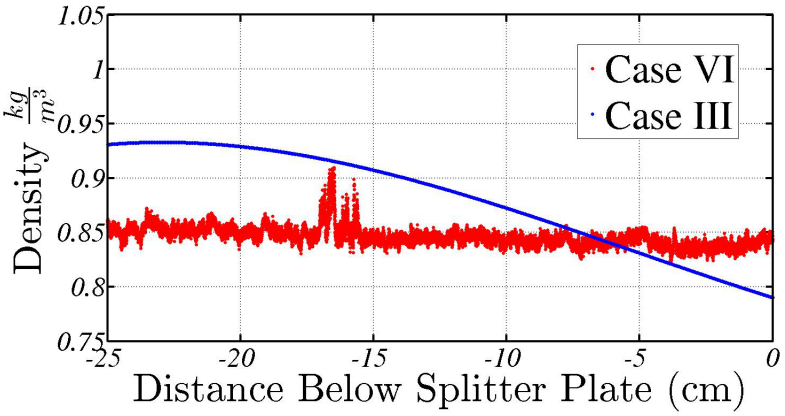

Figure 4.3: Profiles obtained with the density x-probe for Cases III and VI.

4.3 Objective 3

4.3.1 Problem Setup

The third and final objective is to further develop the LLNL K–ε RANS model to use the implicit Crank–Nicolson method and build a foundation for future simulation work. Initial results are obtained from simulating the complex stratification comparison completed for experiments in Objective 2. The development of the code is discussed in detail in § 3.3. To simulate the experiments completed in Objective 2 where the effects of stratification were examined, a third-order best fit curve is used to construct the initial density profile. The density plots shown previously are again given below but scaled for simulation purposes. The corresponding simulation profiles are also given.

To reduce the runtime for the Case IV simulation, the domain size was reduced to a total of 40 cm. This is only done for the low Atwood number case, since the growth of the mixing layer will not be as large as in the other two cases. The domain boundaries are shown in light green in figure 4.4(a), along with the density profiles.

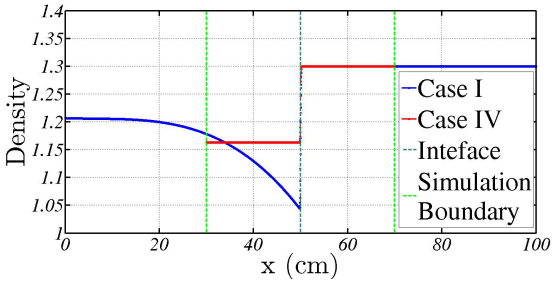

(a) Simulation profile for Case I(a) and IV.

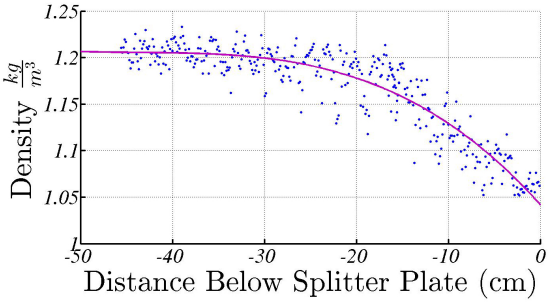

(b) Scaled experimental profile for Case I with third order curve fit for simulation.

Figure 4.4: Case I(a) and IV density profiles used in simulations. The experimental profiles have been scaled in order to match the simulations while keeping the average Atwood number consistent.

In the simulations of Case II(a) and V, the length scale was maintained between the simulations and the experiment by extending the curve at a constant value in figure 4.5(b) beyond 25 *cm* below the splitter plate. Density profile measurements in Case I confirmed the validity of this assumption.

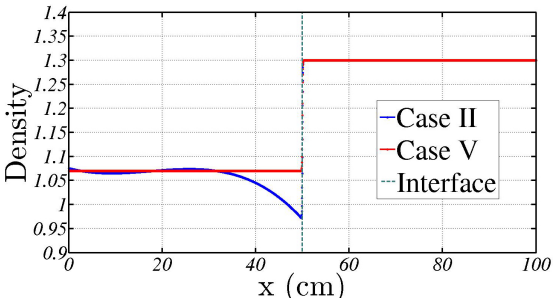

(a) Simulation profile for Case II and V.

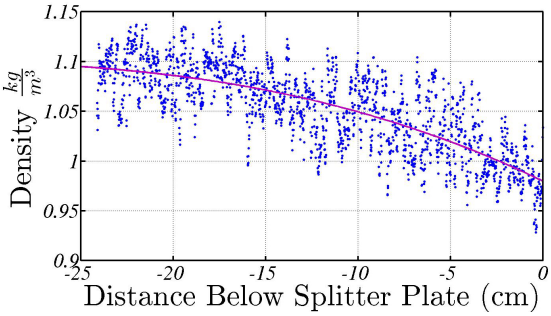

(b) Scaled experimental profile for case II using a third order curve fit.

Figure 4.5: Case II and V density profiles used in simulations. As with Case I, the experimental profile has been scaled to match the simulations while maintaining the correct Atwood number for the simulation.

Finally, the experimental profile is also extended in the simulation for Case III(a) and VI, using the same assumption given in the setup for Case II(a) and V. The simulation initial density profile is given below for both Case III(a) and VI shown in figure 4.6. Again, it should be noted that the curve for Case III(a) does not exactly match the density of Case III(a), but the Atwood numbers do match.

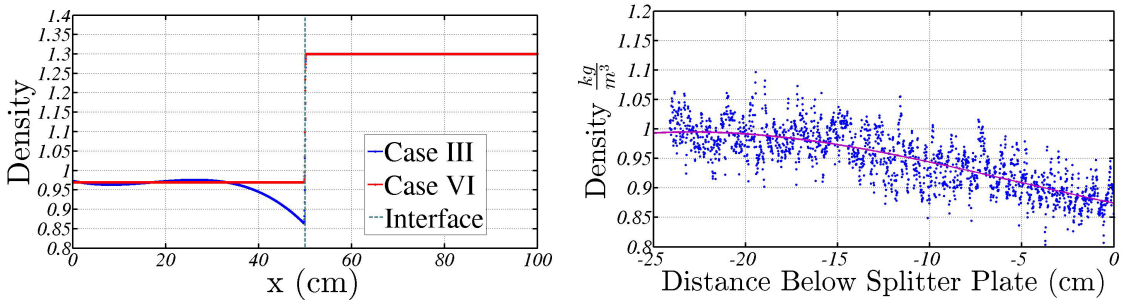

(a) Simulation profile for Case III and VI.

(b) Scaled experimental profile for Case VI.

Figure 4.6: Case III density profiles for simulations.

4.3.2 Simulation Initial Conditions

For this code, the initial conditions are specified for the mean velocity $\tilde{v}$, mean energy $\tilde{e}$, mean heavy mass fraction $\tilde{m}_H$, turbulent kinetic energy K, turbulent kinetic energy dissipation rate ε, and density variance $\overline{\rho'^2}$. The velocity $\tilde{v}$ is set to zero across the domain, and the mean energy is set using equations 3.8 and 3.9 such that

$$\tilde{e} = \frac{\overline{P}}{(\overline{\gamma}-1)\overline{\rho}} + \frac{\tilde{v}^2}{2} + K.$$

The heavy mass fraction is set using an error function profile, which represents the diffusion layer between the streams, while the turbulent kinetic energy and dissipation

rate are initialized by

$$K_0 = K_{mult} PE_{int},$$

$$\varepsilon_0 = K_0 \sqrt{|gA_t| k_{rms}},$$

where K_{mult} is a multiplier set at 0.01, and PE_{int} is the potential energy. In the ε initialization, $k_{rms} = 2\pi/\lambda_{rms}$ where $\lambda_{rms} = 3\,\Delta x$. These are shown together in the figure 4.7.

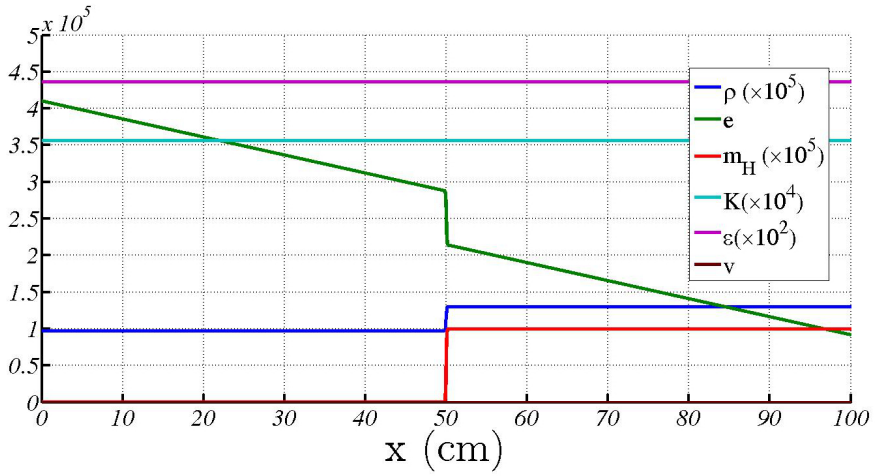

Figure 4.7: Simulation initial conditions for mean density, mean total energy, mean heavy mass fraction, turbulent kinetic energy and turbulent kinetic energy dissipation rate. Gravity is in the negative x direction, and the interface is located at $x = 50\ cm$.

5. EXPERIMENTAL AND MODELING RESULTS WITH DISCUSSION

5.1 Experimental Results

The results from each of these cases will be presented in this section. The mixing layer, growth rate parameter, and mixing layer height gradient in all cases are obtained through image analysis with MATLAB®. Images are taken using the Nikon® D90™ DSLR camera, with the LED backlight. Background images are taken first, followed by fog only and finally fog with helium injection. A total of 100–150 images (depending on experiment) are taken in each set (background, fog only, fog and helium) to ensure statistical convergence, shown in figure 5.1 for the Case I(a) spike growth.

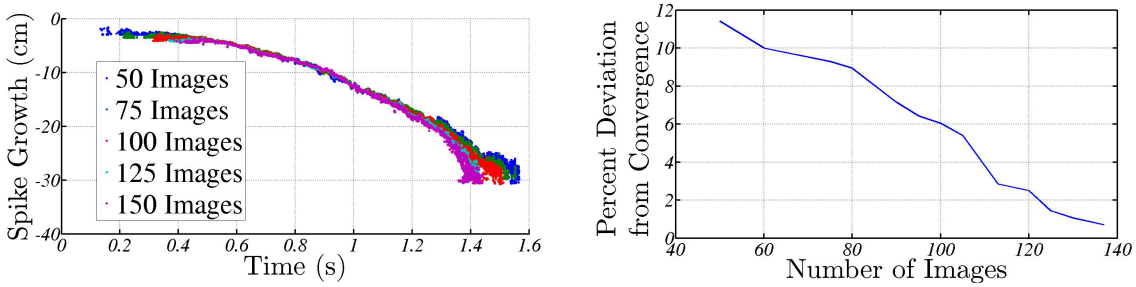

(a) Convergence of spike growth curve for Case I(a).

(b) Maximum percent deviation as a function of the number of averaged images.

Figure 5.1: Image convergence plots. A minimum of 100 images was used in a given experiment (Case III(b) spike). Other experiments use $\sim$ 120–150 images.

In all experiments, 120–150 images were used when averaging (with the exception of the Case III(b) spike, where 100 images were used). This gives a maximum of $\sim$ 2.5% deviation from the converged value. It should also be noted that error bars

are not given in the plots. Since the curve is composed of raw data points, the error associated with mixing width is the thickness of the curve, plus or minus one pixel ($\pm 0.1\ cm$).

Velocity ratios are set and verified with hot-wire and PIV diagnostics prior to running the experiment. Once the images have been captured, they are cropped and averaged, as shown in § 2.2.1. From this image, curves are obtained from the fog concentration. The concentration plot is shown below in figure 5.2 for Case I(a) with profile.

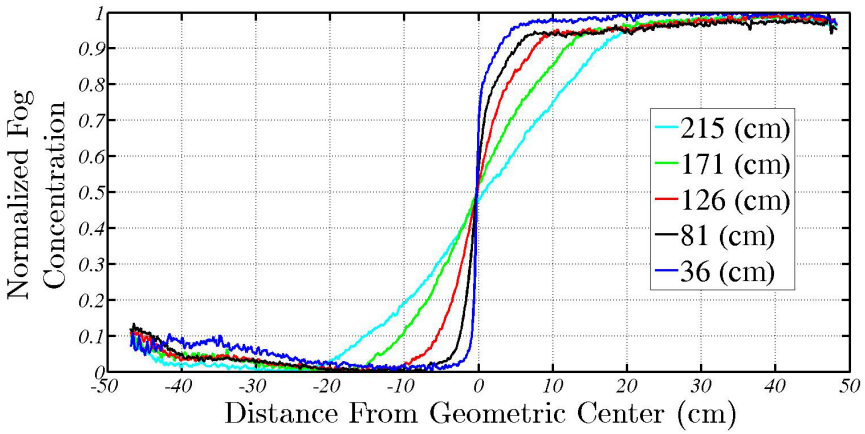

Figure 5.2: Concentration variation along x. As the mixing layer grows further downstream, the concentration gradients are diminished.

Using this curve, values for the mixing width at each downstream location are determined using the 5–95%, which defines the width as the total height between 5% and 95% fog concentration. The averaged image [figure 2.7(b)] is converted to a binary image based on 5% and 95% intensity. The resulting curves correspond to the growth of the bubbles and spikes. Once these curves are obtained, the growth rate parameter, α, and height gradient plots are generated.

As there is inherent shear in the flow field, the growth rate parameter cannot be obtained solely from the helium injection image set. As discussed by Akula *et al.* [6], the total height for the combined instability must be calculated by equation 1.9. Once β is obtained, α is calculated. Banerjee *et al.* [27] discuss numerous ways to calculate α. One such method is the virtual origin (VO) method, first used by Snider and Andrews [22]. Since the boundary layer effects cause a non-zero mixing layer width at the splitter plate, a fictitious point is introduced upstream of the splitter plate where the bubble and spike curves reach zero (thus giving the virtual origin a negative value). A linear curve is then fitted to the mixing layer, where $h = f(A_t g t^2)$. The corresponding slope of this curve is the growth rate parameter $\alpha_{b,s}$. Equation 1.9 is then modified for the VO criteria, and becomes

$$h_{b,s} = \beta\,\Delta U(t - t_0) + \alpha_{VO_{b,s}} A_t\, g(t - t_0)^2, \tag{5.1}$$

where $t = x/U_m$ and U_m is the mean velocity of the flow field.

The second method (RC) used was proposed by Ristorcelli and Clark [49], and was derived using a self-similar analysis resulting in the differential equation

$$\alpha_{RC_{b,s}} = \frac{\dot{h}_{b,s}^2}{4\,A_t\,g\,h_{b,s}} \tag{5.2}$$

For Case IV, both the VO and RC methods were used. Their corresponding plots are shown in figure 5.3 for comparison. Error bars are not given in the figure, since the curves are used for comparison purposes only. Values for the uncertainty associated with $\alpha_{b,s}$ are given at the end of this section.

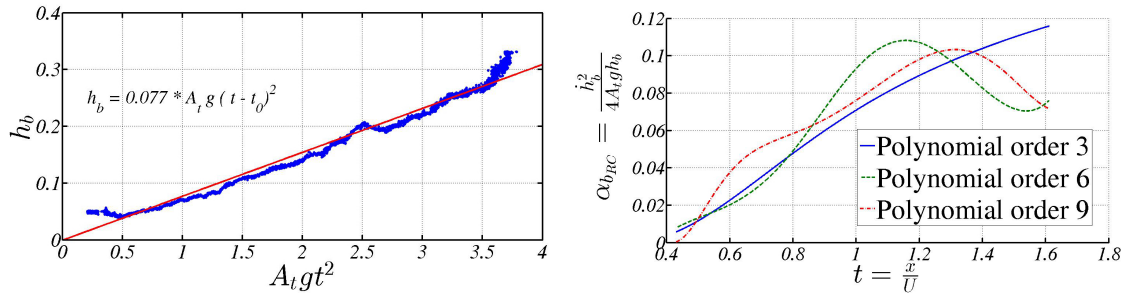

(a) Virtual origin (VO) method for α_b.

(b) Ristorcelli and Clark (RC) method for α_b.

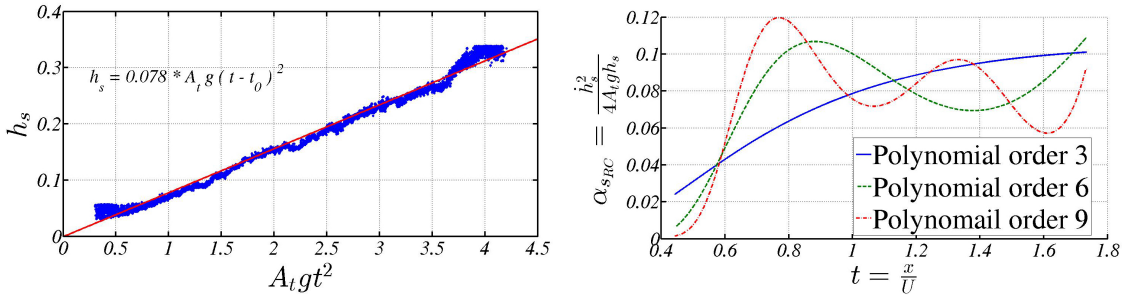

(c) Virtual origin (VO) method for α_s.

(d) Ristorcelli and Clark (RC) method for α_s.

Figure 5.3: Alpha comparison between Virtual Origin (VO) and Ristorcelli and Clark (RC) methods.

From these plots, the slope of the VO curve is similar to the oscillating value from the RC method using a ninth-order polynomial. In fact, Banerjee *et al.* [27] point out that equations 5.1 and 5.2 are actually equal. As a result, and since the calculation of the VO method results in a definitive value, the VO method was used in all alpha calculations to complete the objectives described in § 4.1 through § 4.3.

5.1.1 Objective 1

For Objective 1, Cases I(a,b,c) II(a,b) and III(a,b) will be used to examine the effects of shear on the mixing layer width. In a combined flow, a transition between linear and quadratic growth occurs. To determine the point at which this occurs, the gradient of the bubble mixing height curve is used with a finite difference method to calculate the derivative. Since the transition is from linear to quadratic growth,

transition occurs where a constant curve changes to a linear curve.

The plots for mixing layer width in Case I are given in figure 5.4.

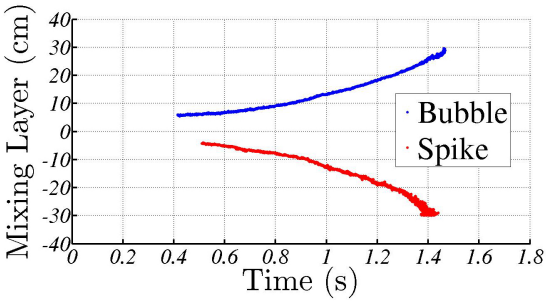

(a) Case I(a) $\Delta U = 0.16\ m/s$.

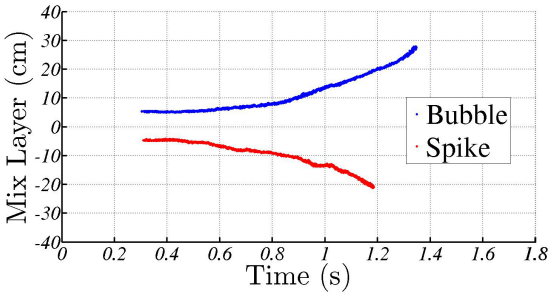

(b) Case I(b) $\Delta U = 0.39\ m/s$.

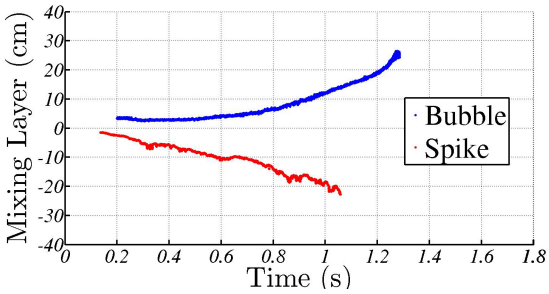

(c) Case I(c) $\Delta U = 0.75\ m/s$.

Figure 5.4: Case I mixing layer widths are compared for each of the ΔU values for $A_t = 0.055$. Early time growth ($t < 0.6\ s$) is reduced as the shear is increased, showing the shear effect inhibiting the growth of the mixing layer. Error bars are not shown for clarity, as the error is the thickness of the curve, $\pm 0.1\ cm$.

The plots shown are constructed from raw data points taken from the averaged digitally processed image mentioned previously in this section. It is noted that the spike curve in 5.4(c) has large error, and therefore is not suitable for calculations or comparison, but is shown for completeness. The point of zero mixing layer is defined as the geometric center of the tunnel, not the center of the mixing layer.

From inspection, late-time quadratic growth can be seen for all cases. Further, the mixing layer growth at times greater than 1 second seems to be unaffected by

the amount of shear in the flow, as all cases show very similar quadratic growth. At times less than 1 second, however, the bubble height is reduced due to the shear, while the spike height is increased. This is most apparent by comparing figures 5.4(a) and 5.4(b). At $t = 0.6\ s$, the mixing layer for Case I(a) is approximately 8 and 5 cm for the bubbles and spikes, respectively. In Case I(b), the bubble height is $\sim 7\ cm$, and the spike height is $\sim 8\ cm$. This growth effect can be explained by the shear pushing the mixing width center below the geometric center (splitter plate) of the tunnel. This trend continues for the bubble curve in Case I(c) figure 5.4(c). It can be seen that this pushing of the mixing layer has caused the early time growth to be symmetric in figure 5.4(b), where it is clearly asymmetric in figure 5.4(a). Plots for the bubble height gradient obtained from the mixing layer curves in figure 5.4 are given in figure 5.5.

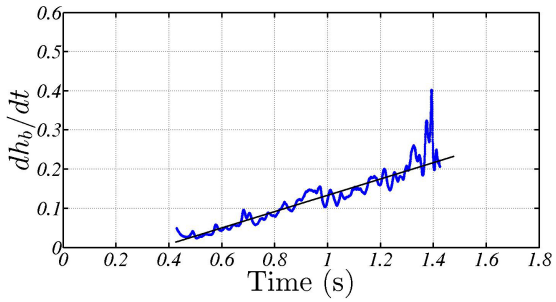

(a) Case I(a) $\Delta U = 0.16\ m/s$.

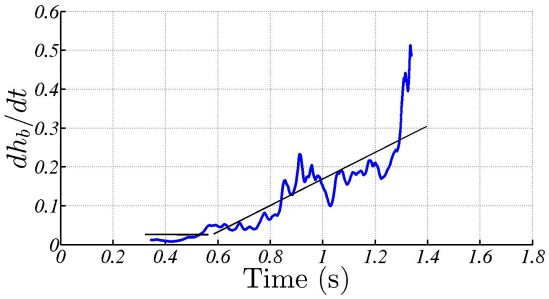

(b) Case I(b) $\Delta U = 0.39\ m/s$.

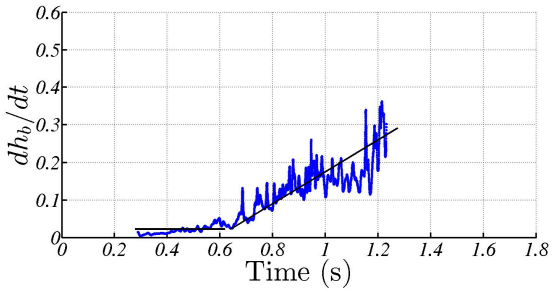

(c) Case I(c) $\Delta U = 0.75\ m/s$.

Figure 5.5: Height gradient plots are given for each of the three mixing layer widths from Case I.

For Case I(a) in figure 5.5(a), the curve agrees well with a linear fit, as expected. This shows no transition, and therefore, the growth of the mixing layer is due to the Rayleigh–Taylor instability rather than to the Kelvin–Helmholtz instability. When more shear is added in figure 5.5(b), there is a region of constant value (0.35–0.6 s). After this constant region, the gradient changes to linear growth, implying quadratic mixing layer growth. This is also seen in the highest shear case, figure 5.5(c), where transition also occurs at about 0.6 s. Table 5.1 shows the transition points and the transitional Richardson number, as calculated by equation 1.7, where the minus sign signifies unstable stratification.

Table 5.1: Case I transition data.

Case	Transition Time (s)	R_i
I(a)	–	–
I(b)	~ 0.55	$(-)0.85-1.13$
I(c)	~ 0.65	$(-)0.23-0.28$

For Cases I(b) and (c), the transitional Richardson numbers fall below the range of -1.5 to -2.5 as stated by Akula *et al.* [6]. The value for Case I(c), however, should not be taken as definitive, as the spike data for Case I(c) has large error as mentioned earlier.

Case II used a higher Atwood number of 0.0971, and due to helium consumption rates, was only tested at two shear ΔU values, 0.25 and 0.94 m/s. The mixing layer plots are given in figure 5.6.

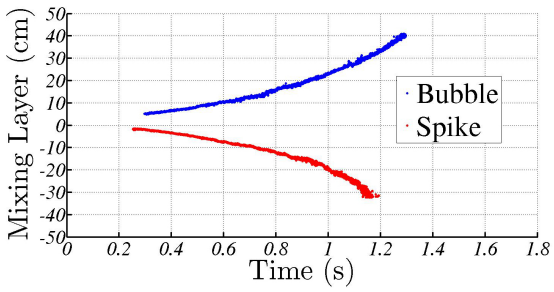

(a) Case II(a) $\Delta U = 0.25\ m/s$.

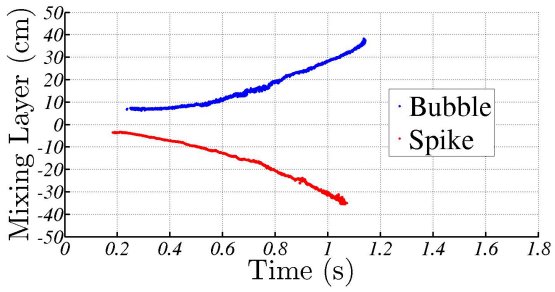

(b) Case II(b) $\Delta U = 0.94\ m/s$.

Figure 5.6: Case II mixing layer widths are compared for each ΔU and $A_t = 0.0971$. Error bars are not given for clarity, the error is the thickness of the curve, $\pm 0.1\ cm$.

With the higher Atwood number of Case II, the mixing layer grows larger in a given amount of time, an obvious result when comparing the mixing layer width for Cases I and II (5.4 and 5.6, respectively). In Case II(a), the growth appears to occur

mostly symmetrically. At 0.8 seconds, the bubble height is larger by a few centimeters than the spike curve, but after this point symmetric growth is re-established, as seen in figure 5.6(a). With shear introduced, the mixing layer grows much faster. At 0.8 seconds, the mixing layer width of Case II(a) is $\sim 26\ cm$, while in Case II(b), this value is $\sim 40\ cm$. At 1 second, the width has increased to ~ 41 and 60 cm for Cases II(a) and (b), respectively. The same effect mentioned in Case I, where the shear seems to produce symmetric early time growth (less than 0.6 s), seems to also be true in Case II.

The gradient plots shown in figure 5.7 also show similar trends to Case I, where the low shear case follows a linear trend close to the beginning of the data set. Additionally, since the Atwood number is higher in Case II, the slope of the linear curve is greater.

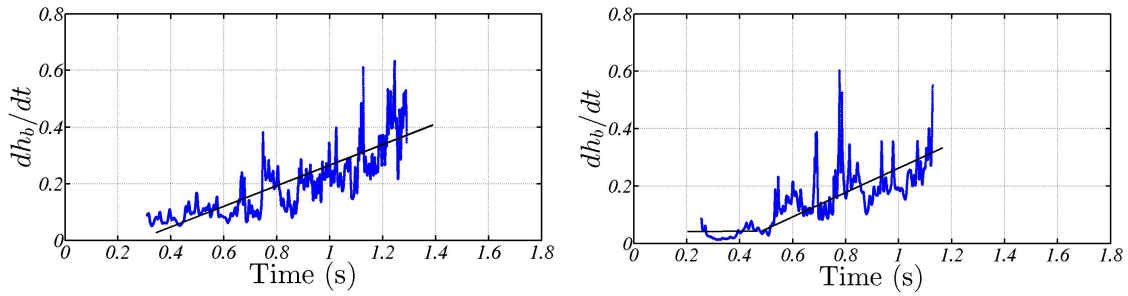

(a) Case II(a) $\Delta U = 0.25\ m/s$.

(b) Case II(b) $\Delta U = 0.94\ m/s$.

Figure 5.7: Case II height gradient.

Finally, the transition point and associated Richardson number are given in table 5.2, which are obtained from figure 5.7. As with Case I(c), the Richardson number is below the -1.5 and -2.5 range.

Table 5.2: Case II transition data.

Case	**Transition Time** (s)	$\boldsymbol{R_i}$
II(a)	–	–
II(b)	~ 0.5	$(-)0.38-0.43$

Finally in Case III, the highest Atwood number was tested with two values $\Delta U =$ 0.27 and 1.0 m/s for sets (a) and (b) respectively. The mixing layer plots are shown in figure 5.8. As expected, the mixing layer grows larger than in the previous two cases.

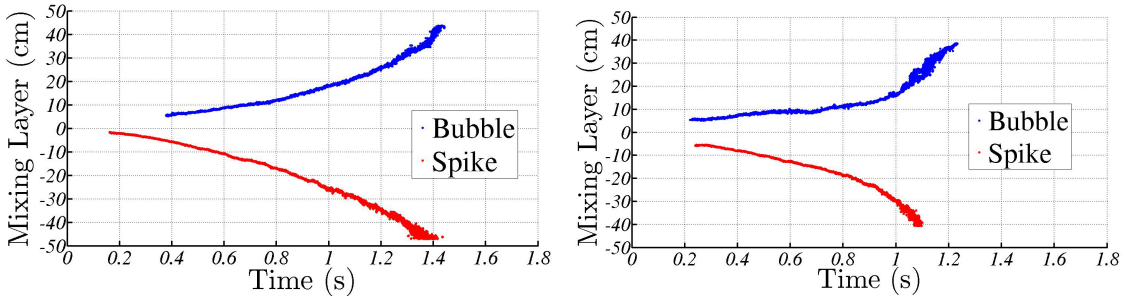

(a) Case III(a) $\Delta U = 0.27\ m/s$.

(b) Case III(b) $\Delta U = 1.0\ m/s$.

Figure 5.8: Case III mixing layer widths for $\Delta U = 0.27\ m/s$ and $1.0\ m/s$ and $A_t =$ 0.147. Error bars are not shown for clarity, and the error corresponds to the thickness of the curve, $\pm 0.1\ cm$.

Asymmetry is also evident in Case III(a) at both early and late times. For Case III(b), early time growth is symmetric, which then transitions to asymmetric growth at later times. The shear effect resulting in early time symmetric growth has been observed in both the previous Cases I and II.

In the general stratification set, bubbles and spikes essentially have the same value for α_b and α_s. However, with complex stratification and some shear, there

is a 11.5% difference between the bubble and spike values. They are also larger, consistent with the trend from the previous two cases.

The figures for the height gradient are given below in figure 5.9. As with Cases I and II before, the low shear case does not clearly demonstrate a transition region. Even though the low shear case still has 0.27 m/s of shear present, the higher Atwood number of 0.147 promotes quadratic growth early on. In the high shear Case III(c), there is an obvious transition point at 0.8 seconds. This is the time used to calculate the transitional Richardson number.

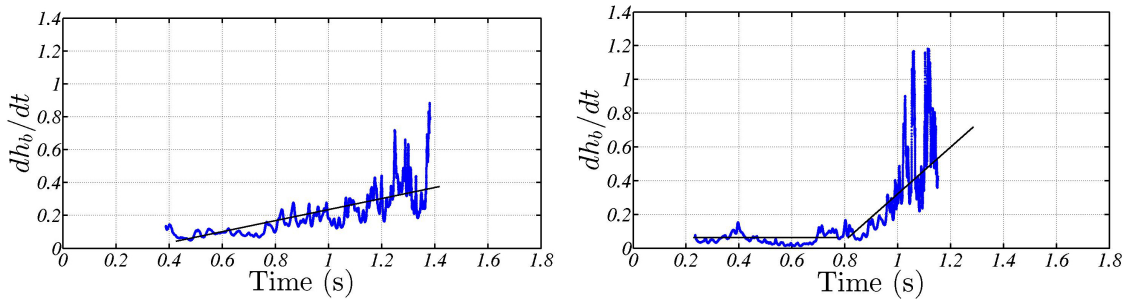

(a) Case III(a) $\Delta U = 0.27\ m/s$.

(b) Case III(b) $\Delta U = 1.0\ m/s$.

Figure 5.9: Case III height gradient.

As stated above, the transitional point and Richardson numbers are measured and calculated using the values obtained at 0.8 seconds and the case parameters given in table 4.1. At the point of transition, the Richardson number was determined to be 0.87, which is again below the range presented by Akula *et al.* [6]. This result is shown in table 5.3.

Table 5.3: Case III transition data.

Case	Transition Time (s)	R_i
III(a)	–	–
III(b)	~ 0.8	$(-)0.86-1.01$

5.1.2 Objective 2

To complete Objective 2, Cases I(a), II(a), and III(a) will be compared to Cases IV, V, VI, respectively, to determine how a complex density profile (or stratification) affects the mixing layer width and the non-dimensional growth parameter $\alpha_{b,s}$. As mentioned at the end of § 5.1, the VO method will be used with β to determine the growth rate parameter using equation 5.1.

Due to the low amounts of helium injected in Case I(a), this case has the largest density variation across the light mixture. The same mixing width plot from Objective 1 is used here, and presented with the corresponding plot from Case IV in figure 5.10.

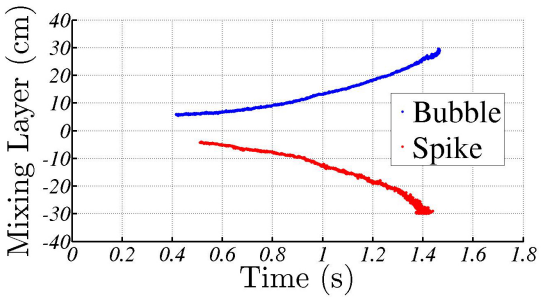

(a) Case I(a) mixing width obtained using a varying density profile (complex stratification) and average Atwood number of 0.055.

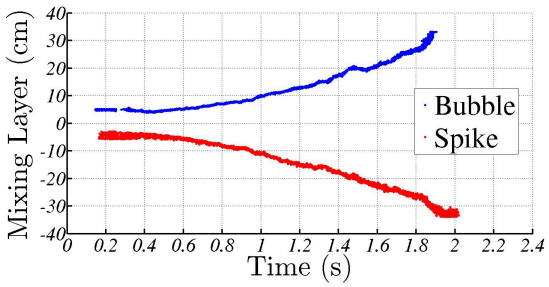

(b) Case IV mixing width obtained using nitrogen injection, which produces a flat density profile (generic stratification) and Atwood number 0.07.

Figure 5.10: Comparison between Cases I(a) and IV, depicting the effect of complex stratification with a low average Atwood number.

In figure 5.10, it is shown that both Case I and IV show symmetric late time growth. This is expected, as the Atwood numbers are sufficiently low ($A_t \lesssim 0.1$). However, Case I(a) shows substantially higher growth than Case IV beyond $\sim$ 1.0–1.1 seconds. At 1.4 seconds, the mixing layer width of Case I(a) reaches $\sim$ 57–58 cm. At the same time for Case IV the mixing layer width is only $\sim$ 38 cm, a 51% difference. This increase in growth will also have an effect on the growth parameter $\alpha_{b,s}$. These values will be presented at the end of this section, where all of $\alpha_{b,s}$ values will be shown for comparison.

The same comparison procedure is used here in Case II(a) and V as above, and the mixing layer plots for Cases II(a) and V are shown in figure 5.11.

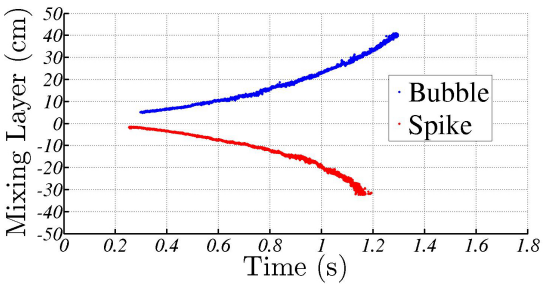

(a) Case II(a) showing mixing layer width for complex stratification with average Atwood number 0.0971.

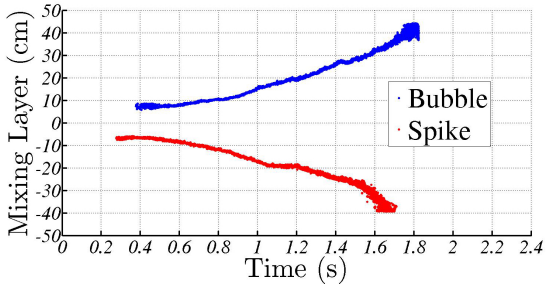

(b) Case V mixing layer width with flat density profile and Atwood number 0.132.

Figure 5.11: Comparison between Cases II(a) and V, showing how complex stratification affects growth with an Atwood number $A_t \sim 0.1$–0.13.

As with the comparison between Cases I(a) and IV, the complex stratified case [Case II(a)] shows faster growth of the mixing layer than the case with the generic profile (Case V). At $\sim$ 1.15 seconds, figure 5.11(a) shows a total mixing layer width of $\sim$ 63 cm while figure 5.11(b) shows a value of $\sim$ 39 cm, a difference of 61%.

The final comparison to complete Objective 2 is between Cases III(a) and VI. The mixing layer plots are shown in figure 5.12.

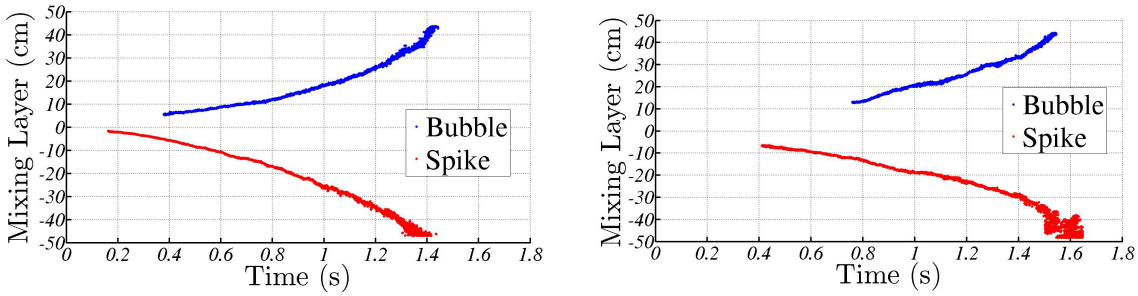

(a) Case III(a) showing mixing width for complex stratification with average Atwood number 0.147.

(b) Case VI mixing width with flat density profile and Atwood number 0.164.

Figure 5.12: Comparison between Cases III(a) and VI, showing how complex stratification affects growth with an Atwood number ~ 0.15.

As expected, similar trends are seen for the highest Atwood case as in the two previous case comparisons. Both spike curves appear to grow non-linearly, as does the bubble curve for Case III(a). It is difficult to draw a conclusion on growth rate from the bubble curve in figure 5.12(b), since only the late-time growth is available. Growth height comparisons, however, can still be made. At 1.35 seconds, the mixing width of Case III(a) is 82 cm, whereas the Case VI mixing width is 60 cm. This is a difference of 37%. This lower percent difference is due to the higher Atwood number. Since the helium is naturally more disperse in the bottom layer, the profile of Case III(a) is closer to its counterpart (Case VI) than any of the other cases.

The non-dimensional growth parameters $\alpha_{b,s}$ for all of the cases compared for Objective 2 will now be discussed and are presented in table 5.4. For comparison purposes, the case numbers are not in sequential order. Since the growth of the mixing width is driven by the light fluid below the splitter plate, the local Atwood number, $A_{t,local}$, is used in the calculation. Uncertainties are obtained using the Kline and McClintock method [63] and shown in parenthesis. Large values of uncertainty are present for Case I(a) and II(a) due to velocity diagnostic issues. These were corrected in subsequent cases, and thus have much less uncertainty. Values for the shear mixing layer growth parameter, β, are obtained using the 5–95% criterion from visualization and equation 1.6.

Table 5.4: Comparison of non-dimensional growth parameter $\alpha_{b,s}$ using local Atwood number below splitter plate. Uncertainty is given in parenthesis.

Case	**Complex Strat.**	$\boldsymbol{A_{t,local}}$	$\boldsymbol{\beta}$	$\boldsymbol{\alpha_b}$	$\boldsymbol{\alpha_s}$
I(a)	YES	0.108	0.324 ($\pm$0.095)	0.096 ($\pm$0.016)	0.164 ($\pm$0.016)
IV	NO	0.070	–	0.078 ($\pm$0.002)	0.078 ($\pm$0.002)
II(a)	YES	0.151	0.358 ($\pm$0.101)	0.110 ($\pm$0.026)	0.147 ($\pm$0.024)
V	NO	0.132	–	0.069 ($\pm$0.002)	0.062 ($\pm$0.002)
III(a)	YES	0.198	0.207 ($\pm$0.012)	0.084 ($\pm$0.002)	0.093 ($\pm$0.003)
VI	NO	0.164	–	0.087 ($\pm$0.002)	0.088 ($\pm$0.002)

Several trends can be seen in table 5.4. The $\alpha_{b,s}$ values are always higher for the cases with complex stratification when compared to the generic case. Generic cases produce growth parameters close to the previously published value of 0.07, while cases with complex stratification, at times, produce values over twice as high. This is consistent with the mixing width results, where the complex stratification caused larger mixing widths at a given time. Another interesting note is that as the

average Atwood number of the complex stratification is increased, the values for α_s are consistently reduced. The same is nearly true for α_b, but the value for Case II(a) is slightly higher than the value in Case I(a).

5.1.3 Objective 3

Objective 3 is completed by implementing the Crank–Nicolson formulation and simulating the cases used for comparison in § 5.1.2. Once the implementation of the Crank–Nicolson formulation (§ 3.3) was completed, the code was validated using the explicit time-evolution formulation. When agreement was confirmed, parametric studies of the time step and number of grid points were conducted, the results of which are shown in figure 5.13.

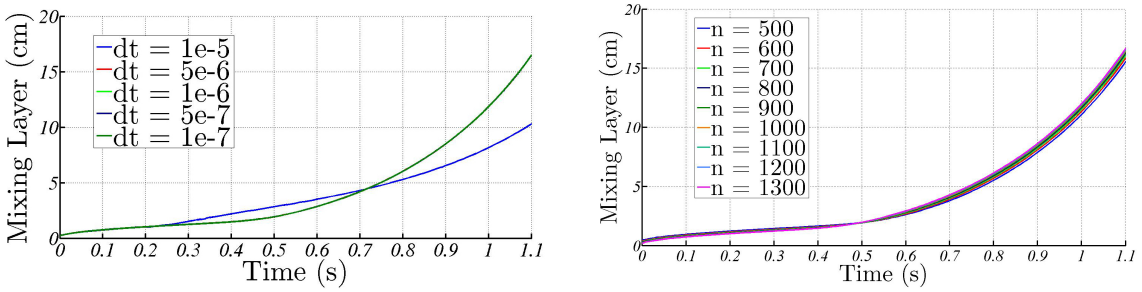

(a) Curves used to determine converged time step. Curves for time steps of 5*e*-6,1*e*-6,5*e*-7, and 1*e*-7 are overlapping.

(b) Curves used to select number of grid points.

Figure 5.13: Time step and grid point study for implicit formulation showing that the mixing widths collapse at $\sim$ 5*e*-6 and $n \sim 1000$. Case VI is shown (generic stratification with $A_t = 0.147$). The domain length of the simulation is 20 cm, corresponding to a Δx of 0.02 cm. From this study, a time step of 5e-6 and a $\Delta x = 0.02$ cm were selected for all simulations, except for Case I(a) and IV, where Δt=1*e*-6 was used.

From figure 5.13(a), it can be concluded that the mixing widths collapse onto the 5*e*-7 curve. Likewise in figure 5.13(b), the curves collapse onto $n = 1000$ points.

Subsequently, a time step of 5e-6 and $\Delta x = 0.020$ have been selected. These values have a maximum deviation of less than 1% and 4%, respectively. The Atwood number is set by inputing the densities of the heavy and light fluids. Further, the gas properties for both the light and heavy fluids are set to the properties of air. Although many quantities can be calculated with the code, only a high level comparison is given in this section. Therefore, the parameters that will be used to relate the experimental and computational data will be the mixing layer width and the self-similar mixing layer growth rate parameter $\alpha_{b,s}$.

Shown below in figure 5.14 are the comparisons for the mixing width from the simulation for an Atwood number of 0.055 between the complex [Case I(a)] and the generic (Case IV) stratification.

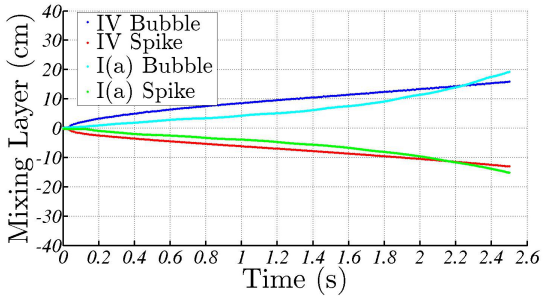

(a) Atwood number 0.055 simulation results for complex and generic stratification.

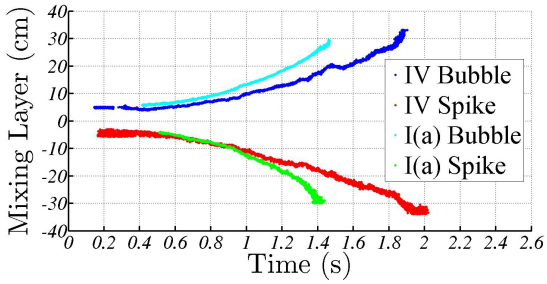

(b) Atwood number 0.055 experimental results for complex and generic stratification.

Figure 5.14: Comparison for simulation and experimental results for complex stratification Case I(a) and generic Case IV, using an Atwood number of 0.055.

Figure 5.14 initially shows a very short diffusion layer for both the generic and profile initial conditions. The generic simulation then transitions to grow at a higher power law rate, where the profile setup does not show this transition, but rather continues to grow in a linear fashion. The curves also grow in a somewhat parallel

manner between 0.5 and 1.25 seconds, where it changes and the profile case seems to grow towards the generic curve.

The most apparent observation from figure 5.14 is that the generic stratification has a larger mixing layer than the complex condition. This is in direct contrast to what was discovered in Objective 2, where the complex stratified case consistently showed higher growth than the generic stratification.

The same VO method used in Objective 2 is used to calculate the growth rate parameter $\alpha_{b,s}$ in Objective 3. These values will be presented together in a table at the end of the section for comparison.

Similar to the previous simulation, a short diffusive regime dominates the growth early on for both the generic and profile initial conditions, and the growth curves appear to overlap early on. The Case II(a) width then begins to grow at a higher rate, a characteristic mimicked by the Case V curve a very short time after. At ~ 1 second, this higher order power law growth terminates, and the self-similar quadratic growth is observed for both curves, with transitioning occurring $\sim 1.25\ s$. With an average Atwood number of 0.0971, the growth of Case II(a) is $\sim 22\%$ greater than that of the Case V.

Plots comparing simulations and experiments for Case II are given below in figure 5.15.

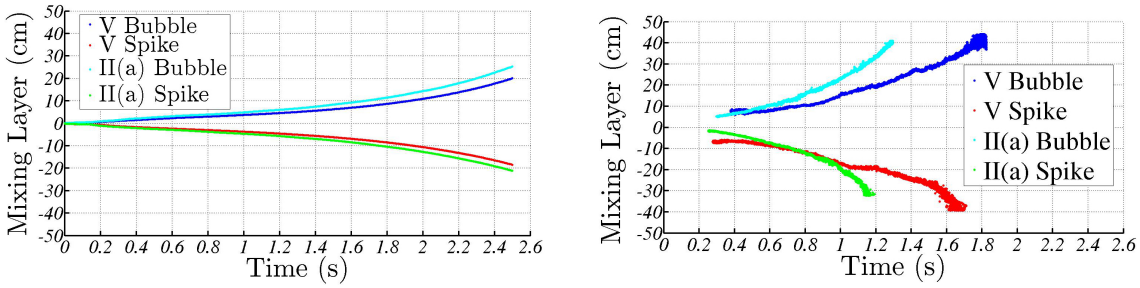

(a) Atwood number 0.0971 simulation results for complex and generic stratification.

(b) Atwood number 0.0971 experimental results for complex and generic stratification.

Figure 5.15: Comparison for simulation and experimental results for complex stratification Case II(a) and generic Case V, with an Atwood number of 0.0971.

Although the plot in figure 5.15 shows the correct trend of the curves with Case II(a) producing a higher growth rate, the simulation is still vastly under predicting the experimental mixing width. At 1 second, the mixing width is at 10 and 8 cm for Case II(a) and V simulations, respectively. From figure 5.11, these values are 41 and 40 cm for experimental Case II(a) and V, respectively.

As with Case II, the initial diffusion layer in Case III grows into a higher power law before turning over into quadratic growth. Again, the complex stratification case [Case III(a)] transitions to the higher order power law sooner than the generic stratification case (Case VI). The transition to self-similar growth occurs at about the same time ($\sim 1.25s$) for both generic and profiled runs.

Finally, the comparison between simulations and experiments for Case III are shown below in figure 5.16.

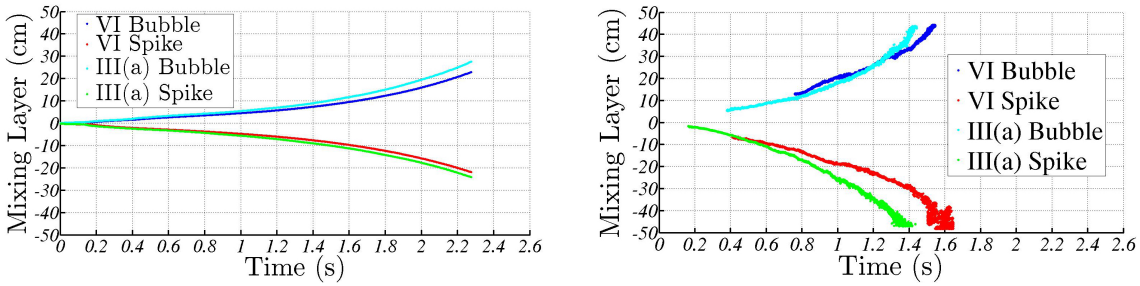

(a) Atwood number 0.147 simulation results for complex and generic stratification.

(b) Atwood number 0.147 experimental results for complex and generic stratification.

Figure 5.16: Comparison for simulation and experimental results for complex stratification Case III(a) and generic Case VI, with an Atwood number of 0.147.

As with the simulations for Case II(a) and V, the simulations in figure 5.16 substantially underpredict the experimental values, although Case III(a) case is correctly showing larger growths than Case VI. Additionally, the difference between the III(a) and VI curves is smaller than the Case II(a) and V curves, $\sim 22\%$ and $\sim 15\%$ respectively.

As done with the experiments used for Objective 2, the growth rate parameter $\alpha_{b,s}$ is presented in table 5.5.

Values for the first simulation of Case I(a) and IV are not given since the curves do not show quadratic growth. The other values in table 5.5 are significantly smaller than the experimental values, which is an expected result since the mixing widths are also under predicted. This could be a result of improper initial conditions. More simulations are required to understand the poor comparisons between the computational and experimental results.

Table 5.5: Comparison of non-dimensional growth parameter from simulations.

Case	**Complex Stratification**	A_t	α_b	α_s
I(a)	YES	0.06	0.037	0.027
IV	NO	0.06	0.002	0.002
II(a)	YES	0.1	0.030	0.024
V	NO	0.1	0.031	0.026
III(a)	YES	0.15	0.029	0.023
VI	NO	0.15	0.026	0.023

5.2 Discussion

From Objective 1, the transition from linear Kelvin–Helmholtz growth to non-linear Rayleigh–Taylor growth is observed. This is a result of the KH vortices dominating the mixing early in time. As time progresses, more fluid is entrained in the vortical structure, producing linear growth. Beyond the point of transition, the buoyancy force dominates the shear, and thus the RT plumes drive the mixing layer growth. When the initial shear is increased (and therefore more energy is input into the system), this transition occurs later in time. The higher energy creates stronger vortices to develop, which then has a stronger hold on the entrained lighter fluid. This ‘‘hold” on the entrained light fluid exceeds the buoyant force, inhibiting the RT growth in early times. As time progresses and more light fluid is entrained, buoyancy forces become larger, and the ‘‘hold” is no longer strong enough to suppress them, resulting in the RT plume structures.

In Objective 2, where the effects of a complex stratification are examined, the mixing layer consistently grows faster than the generic stratification. This is a result of the large buoyancy caused by the pocket of helium located directly below the splitter plate. As time progresses, the light fluid passes through the mixing layer, and the rising pocket defines the bubble height of the mixing width (the corresponding

falling heavy fluid defines the spike growth). Because of the pocket, the local Atwood number below the splitter plate is very high. The average Atwood number, however, is used to calculate the growth parameter $\alpha_{b,s}$. Therefore, the complex stratification $\alpha_{b,s}$ is expected to be higher than the generic stratification value of ~ 0.07.

For Objective 3, simulations were performed on the generic and complex stratifications studied in Objective 2. The simulations show a larger diffusion layer than seen in experiments, and for the early Atwood case, the generic stratification grows faster than the complex stratification. To obtain better simulation results, more quantification of the initial conditions is needed. As Mueschke and Schilling [53] discuss, accurate experimental initial conditions are required in order to perform accurate simulations. One such initial condition that could be determined is the initial wavelength of the perturbation.

6. CONCLUSIONS

This section will now focus on the trends and comparisons observed by completing each of the objectives described above. It is broken down into three parts: discussing the effect of shear on the mixing layer and transition point, the complex versus generic stratification, and finally the simulation of generic and complex stratifications.

6.1 Effects of Shear on Complex Stratification

There are numerous effects that result by adding shear between the stratified layers. The most obvious is that the mixing growth is accelerated with higher amounts of shear. Early time growth is driven by Kelvin–Helmholtz vortical roll ups, which cause linear mixing layer growth. As time progresses, the Rayleigh–Taylor plume structures will dominate these roll ups, resulting in quadratic growth of the mixing layer. As the ΔU between the layers is increased, this transition occurs at later times. The Richardson number is used to quantify this transition, and it was found that transition occurs between the values of -0.25 and -1.0, rather than -1.5 and -2.5 as proposed by Akula *et al.* [6]. This discrepancy in values is expected, as the experiments performed by Akula *et al.* [6] used generic stratification. Thus, using the average Atwood number in equation 1.7 may not be correct for complex stratification, where the high local Atwood number corresponding to the fluid below the splitter plate drives the transition.

It was also observed that the induced shear also promoted symmetrical mixing layer growth at early times. In low shear cases, it was observed that the bubble structures grew faster than the spikes. The shear layer corrects this by pushing the mixing layer down (in the case of the top stream moving faster than the bottom). By lowering the mixing width center, the mixing growth becomes more symmetric.

This was evident in all three comparisons made in § 5.1.1. For low Atwood numbers, the symmetry continues at late times. However, when the Atwood number is higher, asymmetric growth can occur once the mixing is dominated by the Rayleigh–Taylor instability.

6.2 Effects of Stratification

In the experimental cases with a complex stratification, the growth rates are higher for the generic stratification sets, where the $\alpha_{b,s}$ values are much closer to 0.07. The larger growth rates can be attributed to the extremely high density gradient (and therefore local Atwood number) below the splitter plate. This pocket of light fluid located directly below the splitter plate rises through the mixing layer much faster than the fluid in the bottom half of the stream. As the average Atwood number of the case is increased, the values of $\alpha_{b,s}$ seem to agree better with the generic stratification experiment. This is expected, as the profile is not forced but rather created through the natural buoyancy of the lighter fluid. Therefore, as more light fluid is injected, the light fluid pocket will extend further below the splitter plate, which is essentially the generic profile case. As with the equation for Richardson number, using the average Atwood number in equation 5.1 to calculate the growth parameter, $\alpha_{b,s}$, may not be correct. Since the low density fluid below the splitter plate drives the mixing layer growth (and therefore h), using the lower average Atwood number in equation 5.1 results in a higher value of growth parameter, $\alpha_{b,s}$.

6.3 Simulations

The initial simulation results shown in this work did not agree well with experimental data from a numerical comparison. The trends however, were correctly predicted where the complex stratification grew faster than the generic. The disagreement could be a result of improper initial condition implementation, or incorrect model

coefficients given in table 3.1. A parametric study must be performed to determine correct coefficient values. The implicit time evolution scheme must also be tested more rigorously to ensure accuracy.

7. FUTURE WORK

Upon completion of this work, the author will be entering industry. However further progress on this research can be made, which will be discussed in this section.

7.1 Future Experiments

Gas tunnel experiments will continue with the implementation of new diagnostic techniques and the three-layer pure Rayleigh–Taylor experiment. As a result of this research, it has been understood that a new diagnostic technique is required for both accuracy and high Atwood number density measurements. Planar laser induced fluorescence (PLIF) could be a viable alternative to the hot-wire technique. PLIF, however, brings its own set of unique challenges, as discussed further in the appendix. Additionally, the measurement of initial conditions must be performed in order to ensure accuracy of turbulence models.

Another interesting experimental case that will be studied is the three-layer Rayleigh–Taylor instability. The three-layer case has not been well studied, and provides an interesting challenge for both the experimental and computational communities. For the experiments, a third fluid marker must be introduced that is distinguishable from the other two streams.

Finally, experiments testing Atwood numbers greater than 0.6 can be conducted. Before this case can be done, however, the improvements mentioned in the appendix must be addressed. Otherwise, project costs can dramatically increase due to high volumes of helium consumption from re-running experiments.

7.2 Future Code Development

Although improvement has been made, the code can be further developed by converting to two-dimensions and adding parallelization capability to extend the usefulness.

Additionally the Kelvin–Helmholtz problem setup needs to be completed and tested. Once this problem is setup correctly with the one-dimensional code, work can proceed on the combined Rayleigh–Taylor instability. Work has started on simulating the experiments by Bell and Mehta [33], but has yet to be completed or verified.

Since the combined Rayleigh–Taylor and Kelvin–Helmholtz instability problem has velocity components in both x and y directions, the code must be extended to two-dimensions. Although the main equations are already in the code, this conversion will take considerable time and effort. Additionally, with the addition of another dimension, the code inherently becomes more computationally expensive to run. Currently, the code can only run on one node. With a parallelization capability, the wall time could be significantly reduced.

REFERENCES

[1] G. Taylor. The Instability of Liquid Surfaces when Accelerated in a Direction Perpendicular to their Planes. I. *Proceedings of the Royal Society of London. Series A. Mathematical and Physical Sciences*, 201(1065):192--196, 1950.

[2] D. J. Lewis. The Instability of Liquid Surfaces when Accelerated in a Direction Perpendicular to their Planes. II. *Proceedings of the Royal Society of London. Series A*, 202(1068):81--96, 1950.

[3] S. Chandrasekhar. *Hydrodynamic and Hydromagnetic Stability*. Oxford University Press, Oxford, United Kingdom, 1961.

[4] D. L. Youngs. Numerical Simulation of Turbulent Mixing by Rayleigh–Taylor Instability. *Physica D*, 12(1–3):32--44, 1984.

[5] G. Dimonte, D. L. Youngs, A. Dimits, S. Weber, M. Marinak, S. Wunsch, C. Garasi, A. Robinson, M. J. Andrews, P. Ramaprabhu, A. C. Calder, B. Fryxell, J. Biello, L. Dursi, P. MacNeice, K. Olson, P. Ricker, R. Rosner, F. Timmes, H. Tufo, Y.-N. Young, and M. Zingale. A Comparative Study of the Turbulent Rayleigh–Taylor Instability using High-Resolution Three-Dimensional Numerical Simulations: The Alpha-Group Collaboration. *Physics of Fluids*, 16(5):1668--1693, 2004.

[6] B. Akula, M. J. Andrews, and D. Ranjan. Effect of Shear on Rayleigh–Taylor Mixing at Small Atwood Number. *Phys. Rev. E*, 87:033013, 2013.

[7] K. Nagata and S. Komori. The Effects of Unstable Stratification and Mean Shear on the Chemical Reaction in Grid Turbulence. *Journal of Fluid Mechanics*, 408:39--52, 2000.

[8] D.H. Sharp. An Overview of Rayleigh–Taylor Instability. *Physica D*, 12(1–3):3 -- 18, 1984.

[9] J. Imberger and P. F. Hamblin. Dynamics of Lakes, Reservoirs, and Cooling ponds. *Annual Review of Fluid Mechanics*, 14(1):153--187, 1982.

[10] U. Shumlak and N. F. Roderick. Mitigation of the Rayleigh–Taylor Instability by Sheared Axial Flows. *Physics of Plasmas*, 5(6):2384--2389, 1998.

[11] M. H. Emery, J. H. Gardner, and J. P. Boris. Rayleigh–Taylor and Kelvin–Helmholtz Instabilities in Targets Accelerated by Laser Ablation. *Phys. Rev. Lett.*, 48:677–680, 1982.

[12] R. Betti, M. Umansky, V. Lobatchev, V. N. Goncharov, and R. L. McCrory. Hot-Spot Dynamics and Deceleration-Phase Rayleigh–Taylor Instability of Imploding Inertial Confinement Fusion Capsules. *Physics of Plasmas*, 8(12):5257--5267, 2001.

[13] V. A. Thomas and R. J. Kares. Drive Asymmetry and the Origin of Turbulence in an ICF Implosion. *Phys. Rev. Lett.*, 109:075004, 2012.

[14] J. R. Rygg, J. A. Frenje, C. K. Li, F. H. Séguin, R. D. Petrasso, F. J. Marshall, J. A. Delettrez, J. P. Knauer, D. D. Meyerhofer, and C. Stoeckl. Observations of the Collapse of Asymmetrically Driven Convergent Shocks. *Physics of Plasmas*, 15(3), 2008.

[15] O. A. Hurricane, V. A. Smalyuk, K. Raman, O. Schilling, J. F. Hansen, G. Langstaff, D. Martinez, H.-S. Park, B. A. Remington, H. F. Robey, J. A. Greenough, R. Wallace, C. A. Di Stefano, R. P. Drake, D. Marion, C. M. Krauland, and C. C. Kuranz. Validation of a Turbulent Kelvin–Helmholtz Shear Layer

Model Using a High-Energy-Density OMEGA Laser Experiment. *Phys. Rev. Lett.*, 109:155004, 2012.

[16] H. W. Emmons, C.T. Chang, and B.C. Watson. Taylor Instability of Finite Surface Waves. *Journal of Fluid Mechanics*, 7:177--193, 1960.

[17] K. I. Read. Experimental Investigation of Turbulent Mixing by Rayleigh–Taylor Instability. *Physica D*, 12(1–3):45--58, 1984.

[18] M. J. Andrews and D. B. Spalding. A Simple Experiment to Investigate Two Dimensional Mixing by Rayleigh–Taylor Instability. *Physics of Fluids A*, 2(6):922--927, 1990.

[19] P. F. Linden and J. M. Redondo. Molecular Mixing in Rayleigh–Taylor Instability. Part I: Global Mixing. *Physics of Fluids A*, 3(5):1269--1277, 1991.

[20] P. F. Linden, J. M. Redondo, and D. L. Youngs. Molecular Mixing in Rayleigh–Taylor Instability. *Journal of Fluid Mechanics*, 265:97--124, 1994.

[21] S. B. Dalziel, P. F. Linden, and D. L. Youngs. Self-Similarity and Internal Structure of Turbulence Induced by Rayleigh–Taylor Instability. *Journal of Fluid Mechanics*, 399:1--48, 1999.

[22] D. M. Snider and M. J. Andrews. Rayleigh–Taylor and Shear Driven Mixing with an Unstable Thermal Stratification. *Physics of Fluids*, 6(10):3324--3334, 1994.

[23] P. N. Wilson and M. J. Andrews. Spectral Measurements of Rayleigh–Taylor Mixing at Small Atwood Number. *Physics of Fluids*, 14(3):938--945, 2002.

[24] P. Ramaprabhu and M. J. Andrews. Experimental Investigation of Rayleigh–Taylor Mixing at Small Atwood Numbers. *Journal of Fluid Mechanics*, 502:233--271, 2004.

[25] A. Banerjee and M. J. Andrews. Statistically Steady Measurements of Rayleigh–Taylor Mixing in a Gas Channel. *Physics of Fluids*, 18(3):035107, 2006.

[26] W. N. Kraft, A. Banerjee, and M. J. Andrews. On Hot-Wire Diagnostics in Rayleigh–Taylor Mixing Layers. *Experiments in Fluids*, 47(1):49--68, 2009.

[27] A. Banerjee, W. N. Kraft, and M. J. Andrews. Detailed Measurements of a Statistically Steady Rayleigh–Taylor Mixing Layer from Small to High Atwood Numbers. *Journal of Fluid Mechanics*, 659:127--190, 2010.

[28] N. J. Mueschke. *Experimental and Numerical Study of Molecular Mixing Dynamics in Rayleigh–Taylor Unstable Flows*. PhD thesis, Texas A&M Univeristy, College Station, 2008.

[29] N. J. Mueschke, O. Schilling, D. L. Youngs, and M. J. Andrews. Measurements of Molecular Mixing in a High-Schmidt-Number Rayleigh–Taylor Mixing Layer. *Journal of Fluid Mechanics*, 632:17--48, 2009.

[30] H. Görtler. Berechnung von Aufgaben der freien Turbulenz auf Grund eines neuen Näherungsansatzes . *Zeitschrift für Angewandte Mathematik und Mechanik*, 22(5):244--254, 1942.

[31] H. W. Liepmann and J. Laufer. Investigations of Free Turbulent Mixing. *National Advisory Committee for Aeronautics*, (1257), 1947.

[32] A. J. Yule. Two-Dimensional Self-Preserving Turbulent Mixing Layers at Different Free-Stream Velocity Ratios. *Aeronautical Research Council Reports and Memoranda*, (3683), 1971.

[33] J. H. Bell and R. D. Mehta. Development of a Two-Stream Mixing Layer from Tripped and Untripped Boundary Layers. *AIAA Journal*, 28:2034 -- 2042, 1990.

[34] I. Wygnanski and H. E. Fiedler. The Two-Dimensional Mixing Region. *Journal of Fluid Mechanics*, 41:327--361, 1970.

[35] C. D. Winant and F. K. Browand. Vortex Pairing: The Mechanism of Turbulent Mixing-Layer Growth at Moderate Reynolds Number. *Journal of Fluid Mechanics*, 63:237--255, 1974.

[36] F. K. Browand and P. D. Weidman. Large Scales in the Developing Mixing Layer. *Journal of Fluid Mechanics*, 76:127--144, 1976.

[37] M. M. Koochesfahani and P. E. Dimotakis. Mixing and Chemical Reactions in a Turbulent Liquid Mixing Layer. *Journal of Fluid Mechanics*, 170:83--112, 1986.

[38] G. L. Brown and A. Roshko. On Density Effects and Large Structure in Turbulent Mixing Layers. *Journal of Fluid Mechanics*, 64:775--816, 1974.

[39] S. A. Thorpe. A Method of Producing a Shear Flow in a Stratified Fluid. *Journal of Fluid Mechanics*, 32:693--704, 1968.

[40] S. A. Thorpe. Turbulence in Stably Stratified Fluids: A Review of Laboratory Experiments. *Boundary-Layer Meteorology*, 5(1-2):95--119, 1973.

[41] S. A. Thorpe. Experiments on Instability and Turbulence in a Stratified Shear Flow. *Journal of Fluid Mechanics*, 61:731--751, 1973.

[42] F. K. Browand and C. D. Winant. Laboratory Observations of Shear-Layer Instability in a Stratified Fluid. *Boundary-Layer Meteorology*, 5(1-2):67--77, 1973.

[43] C. G. Koop and F. K. Browand. Instability and Turbulence in a Stratified Fluid with Shear. *Journal of Fluid Mechanics*, 93:135--159, 1979.

[44] G. A. Lawrence, F. K. Browand, and L. G. Redekopp. The Stability of a Sheared Density Interface. *Physics of Fluids A*, 3(10):2360--2370, 1991.

[45] D. M. Snider and M. J. Andrews. The Structure of Shear Driven Mixing with an Unstable Thermal Stratificaiton. *Journal of Fluids Engineering*, 118:55--60, 1996.

[46] N. J. Mueschke. An Investigation of the Influence of Initial Conditions on Rayleigh–Taylor Mixing. Master's thesis, Texas A&M University, College Station, 2004.

[47] D. L. Youngs. Three Dimensional Numerical Simulation of Turbulent Mixing by Rayleigh–Taylor Instability. *Physics of Fluids A*, 3(5):1312--1320, 1991.

[48] P. Ramaprabhu and M. J. Andrews. On the Initialization of Rayleigh–Taylor Simulations. *Physics of Fluids*, 16(8):L59--L62, 2004.

[49] J. R. Ristorcelli and T. T. Clark. Rayleigh–Taylor Turbulence: Self–Similar Analysis and Direct Numerical Simulations. *Journal of Fluid Mechanics*, 507:213--253, 2004.

[50] A. Banerjee, R. A. Gore, and M. J. Andrews. Development and Validation of a Turbulent-Mix Model for Variable-Density and Compressible Flows. *Phys. Rev. E*, 82:046309, 2010.

[51] D. M. Snider and M. J. Andrews. The Simulation of Mixing Layers Driven by Compound Buoyancy and Shear. *Journal of Fluids Engineering*, 118:370--376, 1996.

[52] B. J. Olson, J. Larsson, S. K. Lele, and A. W. Cook. Nonlinear Effects in the Combined Rayleigh-Taylor/Kelvin-Helmholtz Instability. *Physics of Fluids*, 23(11):114107, 2011.

[53] N. J. Mueschke and O. Schilling. Investigation of Rayleigh–Taylor Turbulence and Mixing Using Direct Numerical Simulation with Experimentally Measured

Initial Conditions. I. Comparison to Experimental Data. *Physics of Fluids*, 21(1):014106, 2009.

[54] N. J. Mueschke, M. J. Andrews, and O. Schilling. Experimental Characterization of Initial Conditions and Spatio-Temporal Evolution of a Small-Atwood-Number Rayleigh–Taylor Mixing Layer. *Journal of Fluid Mechanics*, 567:27--63, 11 2006.

[55] O. Schilling and N. J. Mueschke. Analysis of Turbulent Transport and Mixing in Transitional Rayleigh–Taylor Ustable Flow Using Direct Numerical Simulation Data. *Physics of Fluids*, 22(10):105102, 2010.

[56] A. Banerjee. *Statistically Steady Measurements of Rayleigh–Taylor Mixing in a Gas Channel*. PhD thesis, Texas A&M University, College Station, 2006.

[57] J. T. Morán-López and O. Schilling. Multicomponent Reynolds Averaged Navier–Stokes Simulations of Reshocked Richtmyer–Meshkov Instability-Induced Mixing. *High Energy Density Physics*, 9(1):112--121, 2013.

[58] J. T. Morán-López and O. Schilling. Multi-Component Reynolds-Averaged Navier–Stokes Simulations of Richtmyer–Meshkov Instability and Mixing Induced by Reshock at Different Times. *Shock Waves*, 24(3):325--343, 2014.

[59] S. B. Pope. *Turbulent Flows*. Cambridge University Press, Cambridge, 2000.

[60] X. Liu, S. Osher, and T. Chan. Weighted Essentially Non-Oscillatory Schemes. *Journal of Computational Physics*, 115(1):200--212, 1994.

[61] H. K. Versteeg and W. Malalasekera. *An Inroduction to Computational Fluid Dynamics: The Finite Volume Method*. Prentice Hall, Upper Saddle River, 2007.

[62] J. W. Buddenberg and C. R. Wilke. Calculation of Gas Mixture Viscosities. *Industrial & Engineering Chemistry*, 41(7):1345--1347, 1949.

[63] S. J. Kline and F. A. McClintock. Describing Uncertainties in Single-Sample Measurements. *Mech. Eng.*, 75:3--8, 1953.

APPENDIX A

IMPROVEMENTS

Throughout the completion of this work, areas of potential improvement were noted with regard to the gas tunnel facility and diagnostic techniques. These improvements and recommendations will now be described with the goal of providing insight to future researchers that will be using this apparatus.

A.1 Gas Tunnel Improvements

The primary hardware component that should be replaced is the suction fan located at the rear of the facility. This fan was recycled from another lab, and does not operate well at low velocities. The air velocity through the fan is changed by adjusting the pitch of the blades inside the fan. When setting the pitch at low angles, the blades can reach an inflection point, and the fan will actually start blowing air rather than sucking it. Additionally, at these low pitch angles, the flow becomes very turbulent as it nears the blades, resulting in larger three-dimensional effects upstream. Furthermore, the pitch adjustment is pneumatically controlled, which lacks precision and requires considerable lag time between adjustments. The pitch also changes as the fan is repeatedly switched on and off over time. To temporarily resolve these problems, the flow velocity is adjusted by moving the fan away from the contraction section. This allows bypass air to be pulled into the fan, reducing the mass flow rate (and consequently velocity) through the tunnel. Given these issues, it is recommended that a fan with a variable frequency drive, or another type of input controller, be used. This will allow greater precision when adjusting flow velocities, and also reduce the setup time between experiments.

In earlier experiments, it was also found that the contraction section immediately upstream of the fan was too close to the test section, imparting three dimensionality into the flow field. To resolve this, a 1.22 m long extension was constructed and placed between the test section and the contraction. This section also has a door for easy entry into the tunnel. Although this extension reduced the effects of the downstream fan and contraction, it was not possible to build it of adequate length due to spatial constraints. When constructing a new section, it is imperative that a door be included. Without this, entry into the tunnel can only be accomplished through the rear of the contraction section, which requires the fan to be moved.

It has also been discovered that mixing in the mixing sections is not as uniform as expected. Currently, a baffle and mixing fan is employed in the mixing section; however, these systems are crude and there is much potential for optimization. It is therefore recommended that a more permanent and properly sized system be designed.

Finally, a new traverse should be installed. Currently, there are two traverse mechanisms: one is located atop the test section and the other must be manually placed inside the tunnel. The traverse located above is too short to span the entire stream-wise length of the test section without significant modification to its mounting base. Furthermore, the required slots that allow the probe to be inserted into the channel were found to induce undesired effects on the flow field. If these slots are to be used, an air tight seal will need to be designed in order to prevent outside air from entering the test section.

The other option is to use the manually inserted traverse. This method allows the slots to be sealed. The traverse, however, is designed for a two-layer facility and does not reach the bottom of the lower stream nor the top of the middle stream. If this method is used in the future, a traverse with a larger throw should be purchased.

A.2 Diagnostic Improvements

Through much experimentation it was discovered that hot-wire anemometry is not the ideal method for measuring the velocity in the flow field. A total of three different probe designs were tested extensively in velocity and density measurements. The probes tested were a Dantec Dynamics three-wire probe, a TSI® film and wire x-probe (referred to as the density probe), and a TSI® three-wire x-probe. The Dantec three-wire probe is capable of measuring all three components of the velocity vector simultaneously. It cannot, however, measure the temperature or the concentration of the fluid. Therefore, it must be outfitted with a constant-current (CCA) probe. The film and wire TSI® probe consists of a thick wire (film) and a thin wire. The film is used to measure concentration, while the wire measures velocity. Since the velocity is measured by this single wire, it is not able to differentiate between velocity in the x and y coordinates, and therefore does not give accurate measurements in a turbulent flow. To circumvent this, the probe was modified by putting a brass sleeve surrounding the wires, which is shown in figure 2.11(a). This effectively eliminated the v component, but still allowed the concentration to be determined. The three-wire TSI® x-probe does allow for u and v velocity components to be measured, and also has a CCA to measure temperature. It does not, however, have a film and therefore cannot measure density.

Without the use of the density probe, a CCA must be present to measure concentrations using a temperature marker technique. This technique can be effective at low Atwood numbers, but is not effective otherwise. Breaking up temperature gradients in the heated stream proved to be difficult. Additionally, adding heat will change the Atwood number of the experiment.

Another issue arises when two gases are present in the test section. The hot-wire

probes cannot differentiate between the new gas and a different velocity, resulting in erroneous data. With the case of helium, this results in higher than expected velocities and lower than expected helium volume fractions. This means that no one single probe can measure all velocity components and the density: multiple probes must be used simultaneously. This requires the design and manufacture of a custom probe mount, and also results in a loss of spatial resolution. Additonally, probes can also be damaged very easily, or fall out of calibration due to a change in BNC cable resistance. This causes considerable time delays for either probe repair or re-calibration.

For these reasons, it is recommended that future users of the facility use optical diagnostics such as PIV and planar laser induced florescence for velocity and concentration measurements, respectively. These diagnostics, however, will provide their own challenges. For example, acetone is currently used as the PLIF tracer. Eventually, acetone will break down the acrylic walls of the test section, resulting in a loss of clarity and possible loss of structural integrity. A new optical arrangement will also need to be developed for PLIF experiments. One suggestion is to place the laser on top of the gas tunnel. Currently, the laser is not powerful enough to fluoresce through an entire seeded fluid stream. Placing the laser on top of the tunnel would then allow the lower stream to be seeded.